INTERNATIONAL JOURNAL FOR NUMERICAL METHODS IN FLUIDS
Int. J. Numer. Meth. Fluids 2004; **44**:347–375 (DOI: 10.1002/fld.641)

Numerical simulation of turbulent free surface flow with two-equation k–ε eddy-viscosity models

V. G. Ferreira[1], N. Mangiavacchi[1], M. F. Tomé[1], A. Castelo[1], J. A. Cuminato[1] and S. McKee[2,*,†]

[1]*Departamento de Ciências de Computação e Estatística, ICMC—Instituto de Ciências Matemáticas e de Computação, USP, São Carlos, SP, Brazil*
[2]*Department of Mathematics, University of Strathclyde, Glasgow, U.K.*

SUMMARY

This paper presents a finite difference technique for solving incompressible turbulent free surface fluid flow problems. The closure of the time-averaged Navier–Stokes equations is achieved by using the two-equation eddy-viscosity model: the high-Reynolds k–ε (standard) model, with a time scale proposed by Durbin; and a low-Reynolds number form of the standard k–ε model, similar to that proposed by Yang and Shih. In order to achieve an accurate discretization of the non-linear terms, a second/third-order upwinding technique is adopted. The computational method is validated by applying it to the flat plate boundary layer problem and to impinging jet flows. The method is then applied to a turbulent planar jet flow beneath and parallel to a free surface. Computations show that the high-Reynolds k–ε model yields favourable predictions both of the zero-pressure-gradient turbulent boundary layer on a flat plate and jet impingement flows. However, the results using the low-Reynolds number form of the k–ε model are somewhat unsatisfactory. Copyright © 2004 John Wiley & Sons, Ltd.

KEY WORDS: averaged Navier–Stokes equations; finite difference; turbulent free surface flow; higher-order upwind bounded scheme; two-equation k–ε eddy-viscosity model

1. INTRODUCTION

Turbulent free surface flows are of great technological interest and yet in 1987 Ferziger [1], in a fairly substantial review on the calculation of incompressible turbulent flows, did not mention this challenging topic. It is interesting to note the changes that have taken place in just 15 years. In 1996 there were no less than three review articles on turbulent free surface flow problems and related topics [2–4]. Other examples of numerical studies of turbulence

*Correspondence to: S. McKee, Department of Mathematics, University of Strathclyde, Livingstone Tower, 26 Richmond Street, Glasgow G1 1XH, U.K.
†E-mail: smck@maths.strath.ac.uk

Contract/grant sponsor: FAPESP; contrat/grant number: 00/03385-0
Contract/grant sponsor: CNPq

Received 19 October 2002
Revised 5 August 2003

Copyright © 2004 John Wiley & Sons, Ltd.

at a free surface include Borue *et al.* [5], Pan and Banerjee [6] and Tsai [7]; all three sets of authors employed the full time-dependent Navier–Stokes and continuity equations, that is direct numerical simulation (DNS). One of the major difficulties is that the free surface boundary conditions are really unknown. This is hardly surprising when one considers the different types of turbulence, as exemplified in the work of Brocchini and Peregrine [8] (and the companion paper, Reference [9]). Almost all modelling, to date (e.g. References [10, 11]), deal with linearized boundary conditions; an exception is Brocchini and Peregrine who discuss free surface boundary conditions for strong turbulence.

How a rigid wall affects turbulence is relatively well understood and, at first sight, it might be thought that these ideas (e.g. law of the wall approximations, etc.) might carry over to free surfaces. However, a free surface can affect turbulence in two ways. First, in the absence of a surface force (e.g. wind), the tangential stresses at the free surface should be zero; near a rigid wall, the velocity gradient is very large which makes turbulence production and dissipation significant there. Secondly, the free surface, at least for weak turbulence, restricts the motion in the normal direction of the flow producing greater lateral movement, while the no-slip boundary condition at a rigid wall makes the velocity components vanish in all directions.

There are many approaches to turbulence modelling: arguably the four main techniques are the two-equation k–ε eddy-viscosity model, Reynolds stress model, large eddy simulation (LES) and DNS. LES calculates the large-scale flow structures of the turbulence explicitly, while modelling the influence of the smaller ones. In DNS, the unaveraged time-dependent Navier–Stokes and continuity equations for turbulent flows are solved numerically. The Reynolds stress model attempts to provide solutions for all components of the Reynolds stress tensor, derived from manipulation of the instantaneous Navier–Stokes equations and Reynolds equations. On the other hand, in the two-equation k–ε turbulence model the basic assumption is that the Reynolds stress tensor can be related to local values of averaged fluid flow variables by introducing a turbulent kinetic energy (k) and a turbulent (or eddy) viscosity (ν_t). The equations must then be closed, and the choice of closure models is itself open to debate. Clearly the advantage of DNS is its independence from any ad-hoc assumptions and its greater flexibility in matching experimental measurements. However, both DNS and LES are still restricted to problems with very small amplitude surface waves, not to mention the usual difficulties associated with a high-Reynolds number flow. Indeed, only wave heights can really be considered that are smaller than the boundary layer thickness.

The two-equation k–ε eddy-viscosity model is still the most widely used in industrial and engineering applications, even though it fails to predict correctly a number of flows. It was developed, calibrated and validated for wall-bounded high-Reynolds number turbulent flows (see References [12, 13]) and has been traditionally used in conjunction with empirical wall functions to patch the core region of the flow to the wall region. However, physical phenomena involved in a free surface flow can be substantially different and have been considered as highly challenging test for validating turbulence models. Furthermore, universal wall functions do not exist for complex flows and this led many authors (in particular, Yang and Shih [14]) to develop a form of k–ε turbulence model that could be integrated down to the wall.

This paper is concerned with adapting the classical front-tracking Marker-and-Cell (MAC) approach (see e.g. Reference [15]) to a two-dimensional variant of the k–ε turbulence model. The two dimensions may be either Cartesian or axisymmetric cylindrical co-ordinates. This adaptation is not straightforward and really depends strongly on recent work of the authors (see e.g. Reference [16]), where upwinding using the variable-order non-oscillatory scheme

Copyright © 2004 John Wiley & Sons, Ltd.

(VONOS) [17] has been applied in addition to a number of other improvements to the original MAC idea (see Reference [18]). In order to validate the numerical method, three fluid flow problems were considered, namely: channel flow, planar jet flow and axisymmetric jet flow. Calculations were carried out for both high and low Reynolds number k–ε eddy-viscosity turbulence models and the results in the case of the high-Reynolds number model displayed good agreement with theoretically derived approximations. Finally, the numerical results of a penetrating planar jet discharging beneath and parallel to a free surface were shown with the ensuing turbulence and how it interacts with the free surface. The paper concludes with some observations and closing remarks.

2. FLUID FLOW EQUATIONS

The conservation equations for two-dimensional time-dependent, viscous, isothermal incompressible turbulent Newtonian fluid flow are the time-averaged Navier–Stokes equations, mass conservation equation, and k and ε equations. In conservative form these fluid flow equations, omitting averaging symbols, can be written, respectively, as

$$\frac{\partial u}{\partial t}+\frac{1}{r^\alpha}\frac{\partial(r^\alpha uu)}{\partial r}+\frac{\partial(uv)}{\partial z}=-\frac{\partial p_e}{\partial r}+\frac{1}{Re}\frac{\partial}{\partial z}\left(\frac{\partial u}{\partial z}-\frac{\partial v}{\partial r}\right)+\frac{1}{Fr^2}g_r + \frac{1}{Re}\left[2\frac{1}{r^\alpha}\frac{\partial}{\partial r}\left(r^\alpha \nu_t\frac{\partial u}{\partial r}\right)+\frac{\partial}{\partial z}\left(\nu_t\left(\frac{\partial u}{\partial z}+\frac{\partial v}{\partial r}\right)\right)-2\alpha\frac{\nu_t u}{r^{2\alpha}}\right] \quad (1)$$

$$\frac{\partial v}{\partial t}+\frac{1}{r^\alpha}\frac{\partial(r^\alpha vu)}{\partial r}+\frac{\partial(vv)}{\partial z}=-\frac{\partial p_e}{\partial z}-\frac{1}{Re}\frac{1}{r^\alpha}\frac{\partial}{\partial r}\left(r^\alpha\left(\frac{\partial u}{\partial z}-\frac{\partial v}{\partial r}\right)\right)+\frac{1}{Fr^2}g_z + \frac{1}{Re}\left[2\frac{\partial}{\partial z}\left(\nu_t\frac{\partial v}{\partial z}\right)+\frac{1}{r^\alpha}\frac{\partial}{\partial r}\left(r^\alpha\nu_t\left(\frac{\partial u}{\partial z}+\frac{\partial v}{\partial r}\right)\right)\right] \quad (2)$$

$$\frac{1}{r^\alpha}\frac{\partial(r^\alpha u)}{\partial r}+\frac{\partial v}{\partial z}=0 \quad (3)$$

$$\frac{\partial k}{\partial t}+\frac{1}{r^\alpha}\frac{\partial(r^\alpha uk)}{\partial r}+\frac{\partial(vk)}{\partial z} =\frac{1}{Re}\left[\frac{1}{r^\alpha}\frac{\partial}{\partial r}\left(r^\alpha(1+\nu_t/\sigma_k)\frac{\partial k}{\partial r}\right)+\frac{\partial}{\partial z}\left((1+\nu_t/\sigma_k)\frac{\partial k}{\partial z}\right)\right]+P-\varepsilon \quad (4)$$

$$\frac{\partial \varepsilon}{\partial t}+\frac{1}{r^\alpha}\frac{\partial(r^\alpha u\varepsilon)}{\partial r}+\frac{\partial(v\varepsilon)}{\partial z}=\frac{1}{Re}\left[\frac{1}{r^\alpha}\frac{\partial}{\partial r}\left(r^\alpha(1+\nu_t/\sigma_\varepsilon)\frac{\partial \varepsilon}{\partial r}\right)+\frac{\partial}{\partial z}\left((1+\nu_t/\sigma_\varepsilon)\frac{\partial \varepsilon}{\partial z}\right)\right] + (C_{1\varepsilon}P-C_{2\varepsilon}\varepsilon)/T_t+\beta E \quad (5)$$

Copyright © 2004 John Wiley & Sons, Ltd.

In the above equations, t is the time, $u=u(r,z,t)$ and $v=v(r,z,t)$ are, respectively, the components in the r and z directions of the local time-averaged velocity vector field $\mathbf{u}=\mathbf{u}(r,z,t)$ of the fluid; $k=k(r,z,t)$ is the local time-averaged turbulent kinetic energy of the fluctuating motion, $\varepsilon=\varepsilon(r,z,t)$ is the turbulence dissipation rate of k, $p_e=p+\frac{2}{3}(1/Re)k$ is the effective scalar pressure field divided by the density, and $\mathbf{g}=(g_r,g_z)$ is the gravitational acceleration. The non-dimensional parameters $Re=U_0L_0/v$ and $Fr=U_0/\sqrt{L_0|\mathbf{g}|}$ denote the associated Reynolds and Froude numbers, respectively, in which U_0 is a characteristic velocity scale, L_0 is a length scale, and v is the kinematic molecular viscosity coefficient. The isotropic eddy viscosity v_t, the turbulent shear stress production P, the turbulence time scale T_t, and the gradient dissipation E are, respectively, defined as

$$v_t=C_\mu f_\mu kT_t \tag{6}$$

$$P=v_t\left(2\left(\frac{\partial u}{\partial r}\right)^2+2\left(\frac{\partial v}{\partial z}\right)^2+2\alpha\left(\frac{u}{r^\alpha}\right)^2+\left(\frac{\partial v}{\partial r}+\frac{\partial u}{\partial z}\right)^2\right) \tag{7}$$

$$T_t=(1-\beta)\,\mathrm{Min}\left\{\frac{k}{\varepsilon},\frac{2}{3C_\mu}\sqrt{\frac{3}{8|\mathbf{S}|^2}}\right\}+\beta\left\{\frac{k}{\varepsilon}+\left(\frac{1}{\varepsilon}\right)^{1/2}\right\} \tag{8}$$

$$E=\frac{2v_t}{Re}\left(\left(\frac{\partial^2 v}{\partial r^2}\right)^2+\left(\frac{\partial^2 u}{\partial z^2}\right)^2\right) \tag{9}$$

where, in (8), $|\mathbf{S}|^2=\mathbf{D}:\mathbf{D}$ [10], with $\mathbf{D}=\frac{1}{2}[\nabla\mathbf{u}+(\nabla\mathbf{u})^{\mathrm{T}}]$. The model constants C_μ, $C_{1\varepsilon}$, $C_{2\varepsilon}$, σ_k and σ_ε, and the parameter β in (5) and (8) are used to specify the two-equation k–ε turbulence models considered in this work. When $C_\mu=0.09$, $C_{1\varepsilon}=1.44$, $C_{2\varepsilon}=1.92$, $\sigma_k=1.0$, $\sigma_\varepsilon=1.3$ and $\beta=0$, we are dealing with the standard high-Reynolds number form of the k–ε model [12] (denoted in this paper by *H Re* k–ε model), with a time scale proposed by Durbin [19] to take account of the stagnation-point anomaly. When the model constants are chosen to be that proposed by Hoffman [20]; that is, $C_\mu=0.09$, $C_{1\varepsilon}=1.81$, $C_{2\varepsilon}=2.0$, $\sigma_k=2.0$, $\sigma_\varepsilon=3.0$ and $\beta=1$, we are treating a low-Reynolds number form of the k–ε turbulence model (denoted here by *L Re* k–ε model) similar to that proposed by Yang and Shih [14]. The damping function f_μ in (6) assumes the value $f_\mu=1$ in the case of the *H Re* k–ε model, and takes the following expression in the case of the *L Re* k–ε model:

$$f_\mu=[1-\exp(-a_1Re_{z_w}-a_3Re_{z_w}^3-a_5Re_{z_w}^5)]^{1/2} \tag{10}$$

where a_1, a_3 and a_5 are constants given by $a_1=1.5\times10^{-4}$, $a_3=5.0\times10^{-7}$, $a_5=1.0\times10^{-10}$ [14], and Re_{z_w} is the local Reynolds number defined as $Re_{z_w}=z_wRe\,k^{1/2}$, z_w being the normal distance from the nearest rigid-boundary to a point in the flow. The parameter α in (1) through (7) is used to specify the co-ordinate system, namely: when $\alpha=0$, plane Cartesian co-ordinates are considered (r is to be interpretted as x and z as y); and when $\alpha=1$, cylindrical polar coodinates are assumed. Equations (1)–(5) have been non-dimensionalized with the following scalings:

$$u^*=uU_0,\quad r^*=rL_0,\quad v^*=vU_0,\quad z^*=zL_0,\quad t^*=tL_0/U_0$$
$$p_e^*=p_eU_0^2,\quad k^*=kvU_0/L_0,\quad \varepsilon^*=\varepsilon vU_0^2/L_0^2,\quad v_t{}^*=v_tv,\quad g_i^*=g_i|\mathbf{g}| \tag{11}$$

where variables with a star refer to their corresponding dimensional variables.

Copyright © 2004 John Wiley & Sons, Ltd.

3. INITIAL AND BOUNDARY CONDITIONS

Equations (1)–(5) are coupled non-linear partial differential equations and, together with the eddy viscosity model (6), are sufficient, in principle, to solve for the five unknowns u, v, p_e, k and ε when appropriate initial and boundary conditions are specified. In this work, a staggered grid is used where the effective pressure, the turbulent kinetic energy and the dissipation rate are stored at the centre of a computational grid cell, while velocities are stored at the cell edges. A typical cell showing the physical locations at which these dependent variables are defined is illustrated in Figure 1. With this grid system, effective pressure boundary conditions are not needed. The boundary conditions and initial conditions have been implemented as follows.

The initial conditions for the mean velocities and effective pressure are specified in the same way as in the laminar case [18, 21]; that is, these variables are prescribed. It can be difficult to specify initial conditions for the turbulent variables since they must be in agreement with the physics of the problem. Thus, for the free surface fluid flow problems considered in this paper, we prescribe the initial conditions for k and ε, and hence v_t, as functions of an upstream turbulent intensity I [22, 23], along with the large-scale characteristic velocity U_0. The variable k is estimated by (see Reference [22])

$$k = k(I, U_0) = IU_0^2 \tag{12}$$

From dimensional reasoning, the variable ε is then determined following [24]

$$\varepsilon = \varepsilon(k, l_t) = \frac{k^{3/2}}{l_t} \tag{13}$$

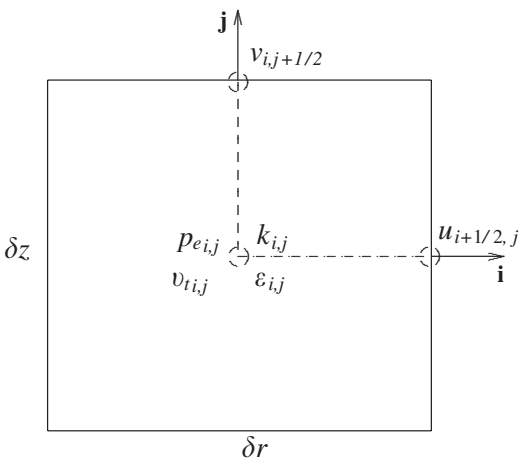

Figure 1. Staggered grid cell showing locations of the dependent variables.

Copyright © 2004 John Wiley & Sons, Ltd.

where l_t is a characteristic length associated with large scales and is chosen as $l_t = \gamma L_0$ [1], with γ a constant. In non-dimensional form, (12) and (13) can be written, respectively, as

$$k = IRe \quad \text{and} \quad \varepsilon = \frac{1}{\gamma}(Re^{-1}k^3)^{1/2} \tag{14}$$

In all computations presented in this paper, the values $I = 8.0 \times 10^{-2}$ and $\gamma = 1.0 \times 10^{-2}$ were employed.

Five types of boundary conditions have been implemented, namely: inflow, outflow, symmetry, free surface, and rigid-wall boundaries. At the inflow, the velocities u and v are prescribed while the values of k and ε are estimated in such a way that they are consistent with the initial conditions (14). At the outflow, the streamwise gradient for each variable is required to be equal to zero. At symmetry boundaries, we set

$$u_n = 0, \quad \frac{\partial u_{\bar{t}}}{\partial n} = 0, \quad \frac{\partial k}{\partial n} = 0 \quad \text{and} \quad \frac{\partial \varepsilon}{\partial n} = 0 \tag{15}$$

where n and $\bar{t}$ denote normal and tangential directions to the boundary, respectively. At a free surface, we consider the fluid to be moving into (or out of) a passive atmosphere (zero-pressure) and, in the absence of surface tension forces, the normal and tangential components of the stress must be continuous across any free surface; hence on such a surface we have (see, for example, Reference [26])

$$\mathbf{n} \cdot (\boldsymbol{\tau} \cdot \mathbf{n}) = 0 \tag{16}$$

$$\mathbf{m} \cdot (\boldsymbol{\tau} \cdot \mathbf{n}) = 0 \tag{17}$$

Here, $\mathbf{n}$ and $\mathbf{m}$ are unit normal and tangential vectors to the surface, and $\boldsymbol{\tau} = \boldsymbol{\tau}(p_e, v_t, \mathbf{u})$ is the Cauchy stress-tensor defined by

$$\boldsymbol{\tau} = -p_e \mathbf{I} + Re^{-1}(1 + v_t)\mathbf{D} \tag{18}$$

where $\mathbf{I}$ denotes the identity tensor. Following the approach in Reference [21], Equations (16) and (17) are discretized by accurate local finite difference approximations on the free surface, namely: from condition (16) one determines the effective pressure; and from (17) one obtains the velocities at the free surface. Due to the complexity of the dynamics of the turbulence near to the interface, the values of the turbulent variables k and ε at the free surface of the fluid are difficult to specify. For instance, it is not known how turbulence interacts with the surface tension and, therefore, it is difficult to specify the distribution of k on an irregular moving free surface. So, as a first approximation, we assume that the free surface is locally flat and the movement of the fluid does not cause any discontinuities at this boundary. In summary, the turbulent variables at the free surface are determined by imposing

$$\frac{\partial k}{\partial n} = 0 \quad \text{and} \quad \frac{\partial \varepsilon}{\partial n} = 0 \tag{19}$$

The derivatives in (19) are approximated by first-order finite differences.

The boundary conditions at a rigid-wall depend on the k–ε viscosity model under consideration. When the simulation is performed with the *H Re* k–ε model, the wall function approach

Copyright © 2004 John Wiley & Sons, Ltd.

is employed. In this case, the fundamental equation for determining the fictitious velocities and turbulent variables near a rigid wall is the total wall shear stress (or momentum flux) τ_w given by [23]

$$\left(Re^{-1}(1+\nu_t)\left|\frac{\partial \hat{u}}{\partial n}\right|\right)\Bigg|_{\text{wall}} \approx u_\tau^2 = \tau_w \tag{20}$$

where $\hat{u}$ represents the mean velocity component tangential to the rigid-wall, and u_τ is the friction velocity. The values of the k and ε in the inertial sublayer are, respectively, prescribed by the well known relations [23, 27]

$$k = Re\,\frac{\tau_w}{C_\mu^{1/2}} \quad \text{and} \quad \varepsilon = Re\,\frac{\tau_w u_\tau}{K z_w} \tag{21}$$

where $K = 0.41$ is the von Kármán constant (see, for example, Reference [28]). In the viscous region close to the wall (viscous sublayer), we use the strategy of Sondak and Pletecher [27]; that is,

$$k = Re\,\frac{\tau_w}{C_\mu^{1/2}}\left(\frac{z^+}{z_c{}^+}\right)^2 \quad \text{and} \quad \varepsilon = Re^{-1/2}\,\frac{k^{3/2}}{l^*} \tag{22}$$

where z^+ is defined as $z^+ = Re\,u_\tau z_w$, and l^* represents the length scale proposed by Norris and Reynolds [29]. Neglecting the buffer layer of the turbulent boundary layer, the critical value of z^+ (denoted by $z_c{}^+$) in (22) separates the viscous sublayer from the inertial sublayer. A detailed discussion of the initial and boundary conditions for the $H\,Re$ k–ε turbulence model can be found in Ferreira [30]. When the $L\,Re$ k–ε model is used, the velocity at the solid boundary is set to zero to represent the no-slip velocity boundary condition ($\mathbf{u} = \mathbf{0}$), and the values of the turbulent quantities k and ε at the wall are specified, respectively, as [31]:

$$k_w = 0 \quad \text{and} \quad \varepsilon_w = 2Re^{-1}\left(\frac{\partial k^{1/2}}{\partial n}\right)^2 \tag{23}$$

3.1. Implementation of wall functions

It is well established by now that the $H\,Re$ k–ε model requires to be modified so that flow simulations near rigid boundaries can take account of the damping of velocity fluctuations and the viscous effects. In general, the solution of the k–ε conservation equations in the inner layer of a turbulent boundary layer near the wall is not necessary since the flow mechanism in such a region can be described reasonably well by employing wall functions (for a more detailed discussion see, for example, Reference [30]). In what follows, we describe our implementation of the law of the wall boundary conditions.

The behavior of the mean velocity profiles in the viscous and inertial sublayers are, respectively, given by (see, for example, References [32–34])

$$u^+ - z^+ = 0 \tag{24}$$

$$ln(Ez^+) - Ku^+ = 0 \tag{25}$$

Copyright © 2004 John Wiley & Sons, Ltd.

where $u^+ = \hat{u}/u_\tau$ and $E = \exp(KB)$; B is an empirical constant and is usually chosen to correspond to a hydrodynamically smooth wall [26]. One of the central questions in the application of the wall functions (20)–(22) and (24)–(25) is the accurate determination of the friction velocity, and hence the wall shear stress. This is determined from the relations (24) or (25), depending on the local Reynolds number z^+. To obtain u_τ from (25), Newton–Raphson is applied; a choice of the initial starting guess $u_\tau = 11.60$ was employed by Benim and Zimer [35]. To begin with, we need to know the critical Reynolds number z_c^+; this is a measure of the (non-dimensional) distance separating the viscous sublayer from the inertial sublayer. By neglecting the transition sublayer (buffer layer), the friction velocity is estimated in the following manner: with the tangential velocity $\hat{u}$ known in the first grid cell adjacent to the wall, u_τ is updated according to the value of z^+ given by (24). If z^+ is less than z_c^+, we use (24); on the other hand, if it is not, we employ (25). The fictitious velocities are calculated by the central-difference approximation of (20) for a known wall shear stress.

4. SOLUTION TECHNIQUE

The governing equations (1) through (5) are solved with an extension of the GENSMAC methodology for the turbulent flow field (see Reference [30]). A detailed description of this code for a laminar flow field is provided by Tomé and McKee [18] and Tomé *et al.* [21]. Based on a predictor-corrector scheme, GENSMAC is an explicit finite difference, first/second-order accurate numerical method for the calculation of free-surface flows as well as confined flows. By using a guessed effective pressure $\tilde{p}_e$ and an eddy viscosity ν_t, the method consists of solving the time-averaged Navier–Stokes equations at the $(k+1)$ time-step for an intermediate velocity field $\tilde{\mathbf{u}}$. The $\tilde{\mathbf{u}}$ velocity is related to the true velocity field $\mathbf{u}$, at the $(k+1)$ time-step, by an auxiliary potential function ψ which is calculated from a Poisson equation, obtained by imposing $\nabla \cdot \mathbf{u} = 0$ at the $(k+1)$ time-step. The effective pressure and the turbulent variables k and ε are then updated and the procedure is repeated at each time-step. In particular, when calculating $\tilde{\mathbf{u}}$ in step 1 we employ an adaptive time-stepping routine (see Reference [18]). The numerical solution procedure may be summarized as follows.

It is supposed that, at a given time $t = t_0$, the velocity field $\mathbf{u}$ is known and suitable boundary conditions for the velocity and turbulent variables are given. Let $\tilde{p}_e(r,z,t)$ be an arbitrary effective pressure field that satisfies the correct pressure condition on the free surface. This pressure field is constructed employing the normal-stress condition (16) at the free surface, and is chosen arbitrarily (for instance, $\tilde{p}_e(r,z,t) = 0$) within the fluid. The updated velocity field, the effective pressure and the turbulent variables are calculated at time $t = t_0 + \delta t$ by the following steps:

1. With the eddy viscosity ν_t known at $t = t_0$, compute an approximate velocity field $\tilde{\mathbf{u}}(r,z,t) = [\tilde{u}(r,z,t), \tilde{v}(r,z,t)]$ from an explicit finite difference discretization of

$$\left.\frac{\partial \tilde{u}}{\partial t}\right|_{t=t_0} = \left\{ -\frac{1}{r^\alpha}\frac{\partial (r^\alpha uu)}{\partial r} - \frac{\partial (uv)}{\partial z} - \frac{\partial \tilde{p}_e}{\partial r} + \frac{1}{Re}\frac{\partial}{\partial z}\left(\frac{\partial u}{\partial z} - \frac{\partial v}{\partial r}\right) + \frac{1}{Fr^2}\, g_r \right.$$
$$\left. + \frac{1}{Re}\left[2\,\frac{1}{r^\alpha}\frac{\partial}{\partial r}\left(r^\alpha \nu_t \frac{\partial u}{\partial r}\right) + \frac{\partial}{\partial z}\left(\nu_t \left(\frac{\partial u}{\partial z} + \frac{\partial v}{\partial r}\right)\right) - 2\alpha\,\frac{\nu_t u}{r^{2\alpha}}\right] \right\}\Bigg|_{t=t_0} \qquad (26)$$

Copyright © 2004 John Wiley & Sons, Ltd.

$$\left.\frac{\partial \tilde{v}}{\partial t}\right|_{t=t_0} = \left\{ -\frac{1}{r^\alpha}\frac{\partial (r^\alpha vu)}{\partial r} - \frac{\partial (vv)}{\partial z} - \frac{\partial \tilde{p}_e}{\partial z} - \frac{1}{Re}\frac{1}{r^\alpha}\frac{\partial}{\partial r}\left(r^\alpha\left(\frac{\partial u}{\partial z} - \frac{\partial v}{\partial r}\right)\right) + \frac{1}{Fr^2}g_z \right.$$
$$\left. + \frac{1}{Re}\left[2\frac{\partial}{\partial z}\left(\nu_t\frac{\partial v}{\partial z}\right) + \frac{1}{r^\alpha}\frac{\partial}{\partial r}\left(r^\alpha \nu_t\left(\frac{\partial u}{\partial z} + \frac{\partial v}{\partial r}\right)\right)\right]\right\}\Bigg|_{t=t_0} \tag{27}$$

with $\tilde{\mathbf{u}}(r,z,t_0) = \mathbf{u}(r,z,t_0)$ using the correct boundary conditions for $\mathbf{u}(r,z,t_0)$. It can be shown (see, for example, Reference [21]) that $\tilde{\mathbf{u}}(r,z,t)$ possesses the correct vorticity at time t but does not satisfy (3), in general. By writing

$$\mathbf{u}(r,z,t) = \tilde{\mathbf{u}}(r,z,t) - \nabla\psi(r,z,t) \tag{28}$$

and imposing

$$\nabla^2\psi(r,z,t) = \nabla\cdot\tilde{\mathbf{u}}(r,z,t) \tag{29}$$

a velocity field is obtained in which the vorticity and mass are conserved.

2. Solve the Poisson equation (29) for potential function ψ. The appropriate boundary conditions for this elliptic equation are homogeneous Dirichlet-type on the free surface and homogeneous Neumann-type on the fixed boundaries [36]. These are treated in a similar way as in the GENSMAC code of References [18, 21].
3. Calculate the velocity field $\mathbf{u}(r,z,t)$ from (28).
4. Compute the effective pressure. It can be shown (see Reference [30]) that this pressure field is given by

$$p_e(r,z,t) = \tilde{p}_e(r,z,t) + \psi(r,z,t)/\delta t \tag{30}$$

5. Compute the kinetic energy k from an explicit finite difference approximation of (4).
6. Compute the dissipation rate ε from an explicit finite difference approximation of (5).
7. Update the eddy viscosity ν_t from (6).
8. Particle movement. The last step in the calculation involves the movement of the marker particles to their new positions. These are virtual particles (without mass, volume, or other properties), whose co-ordinates are stored and updated at the end of each cycle by solving the ordinary differential equations

$$\dot{r} = u(r,z,t) \quad \text{and} \quad \dot{z} = v(r,z,t) \tag{31}$$

by Euler's method. This provides the particles with new co-ordinates, thus determing whether or not an individual particle has moved into a new computational cell, or if it has left the containment region through an outflow boundary.

In order to improve efficiency particles are only defined on the fluid boundary. This is achieved by using a set of ordered lists defining the interior of the fluid region. Each list stores connected information about the type of movement the particle is entitled to make. For instance, a particle of type 'inflow' cannot move, whereas a particle of type 'surface' can move freely according to the computed velocity field. The fluid surface (hence the free surface) is obtained by connecting these particles by straight lines. A procedure for inserting/deleting particles is employed. Should the distance between any two particles be greater than that d_u (usually about 0.6 of the cell length) a particle is inserted midway between the two particles on the line joining them. On the other

Copyright © 2004 John Wiley & Sons, Ltd.

hand, if the distance between any two particles is less than d_L (usually about $\frac{1}{20}$ of the cell length), these two particles are replaced by a single particle at the mid-point of the line joining them. Details of the free surface treatment are given in Tome *et al.* [21].

9. Update the boundary conditions and go back to the first step.

5. DISCRETIZATION OF THE FLUID FLOW EQUATIONS

In the solution procedure described in the previous section, the differential equations were discretized using a finite difference formulation on a uniform staggered grid. The temporal derivatives were discretized using the first-order forward difference (Euler's method), while the spatial derivatives were approximated by standard second-order central differences with the exception of the convection terms (denoted here by CONV$(\cdot)$), which were handled with the VONOS scheme of Varonos and Bergeles [17]. This is a second/third-order accurate upwind differencing scheme that satisfies the convection boundedness criterion (CBC) proposed by Gaskell and Lau [37]. For details of implementation and application of this advection scheme in laminar free surface flows, the reader is referred to Ferreira *et al.* [16]. The Poisson equation (29) is discretized using the usual five-point Laplacian operator and the resulting symmetric positive definite linear system is solved by the conjugate-gradient method. In summary the fluid flow equations (1)–(5) take the following discretized form:

- *r-Momentum*

$$\begin{aligned}\tilde{u}^{k+1}_{i+1/2,j} = u^k_{i+1/2,j} + \delta t \Bigg\{ & \mathrm{CONV}(u)|_{i+1/2,j} - (p_{\mathrm{e}i+1,j} - p_{\mathrm{e}i,j})/\delta r \\ & + \frac{1}{Re\,\delta z}[((u_{i+1/2,j+1} - u_{i+1/2,j})/\delta z - (v_{i+1,j+1/2} - v_{i,j+1/2})/\delta r) \\ & - ((u_{i+1/2,j} - u_{i+1/2,j-1})/\delta z - (v_{i+1,j-1/2} - v_{i,j-1/2})/\delta r)] \\ & + \frac{2}{Re\, r^{\alpha}_{i+1/2,j}\,\delta r^2}(r^{\alpha}_{i+1,j} v_{ti+1,j}(u_{i+3/2,j} - u_{i+1/2,j}) - r^{\alpha}_{i,j} v_{t_{i,j}}(u_{i+1/2,j} - u_{i-1/2,j})) \\ & + \frac{1}{Re\,\delta z}[v_{ti+1/2,j+1/2}((u_{i+1/2,j+1} - u_{i+1/2,j})/\delta z + (v_{i+1,j+1/2} - v_{i,j+1/2})/\delta r) \\ & - v_{ti+1/2,j-1/2}((u_{i+1/2,j} - u_{i+1/2,j-1})/\delta z + (v_{i+1,j-1/2} - v_{i,j-1/2})/\delta r)] \\ & - \frac{2\alpha}{Re\, r^{2\alpha}_{i+1/2,j}} v_{ti+1/2,j} u_{i+1/2,j} + \frac{1}{Fr^2} g_r \Bigg\}^k \end{aligned} \tag{32}$$

where the superscript k denotes the time level, and

$$\mathrm{CONV}(u)|^k_{i+1/2,j} = \left[\frac{1}{r^{\alpha}}\frac{\partial(r^{\alpha} uu)}{\partial r} + \frac{\partial(uv)}{\partial z}\right]\Bigg|^k_{i+1/2,j} \tag{33}$$

Copyright © 2004 John Wiley & Sons, Ltd.

• *z-Momentum*

$$\tilde{v}^{k+1}_{i,j+1/2} = v^k_{i,j+1/2} + \delta t \left\{ \mathrm{CONV}(v)|_{i,j+1/2} - (p_{\mathrm{e}i,j+1} - p_{\mathrm{e}i,j})/\delta z \right.$$
$$- \frac{1}{Re\,\delta r r^\alpha_{i,j+1/2}} [r^\alpha_{i+1/2,j+1/2}((u_{i+1/2,j+1} - u_{i+1/2,j})/\delta z - (v_{i+1,j+1/2} - v_{i,j+1/2})/\delta r)$$
$$- r^\alpha_{i-1/2,j+1/2}((u_{i-1/2,j+1} - u_{i-1/2,j})/\delta z - (v_{i,j+1/2} - v_{i-1,j+1/2})/\delta r)]$$
$$+ \frac{2}{Re\,\delta z^2}(v_{ti,j+1}(v_{i,j+3/2} - v_{i,j+1/2}) - v_{ti,j}(v_{i,j+1/2} - v_{i,j-1/2}))$$
$$+ \frac{1}{Re\,\delta r r^\alpha_{i,j+1/2}} [r^\alpha_{i+1/2,j+1/2} v_{t_{i+1/2,j+1/2}}((u_{i+1/2,j+1} - u_{i+1/2,j})/\delta z + (v_{i+1,j+1/2} - v_{i,j+1/2})/\delta r)$$
$$- r^\alpha_{i-1/2,j+1/2} v_{ti-1/2,j+1/2}((u_{i-1/2,j+1} - u_{i-1/2,j})/\delta z + (v_{i,j+1/2} - v_{i-1,j+1/2})/\delta r)]$$
$$\left. + \frac{1}{Fr^2} g_z \right\}^k \tag{34}$$

where

$$\mathrm{CONV}(v)|^k_{i,j+1/2} = \left[\frac{1}{r^\alpha} \frac{\partial (r^\alpha v u)}{\partial r} + \frac{\partial (v v)}{\partial z} \right] \Bigg|^k_{i,j+1/2} \tag{35}$$

• *Poisson equation for* ψ

$$\frac{1}{r^\alpha_{i,j}\delta r^2}(r^\alpha_{i+1/2,j}(\psi_{i+1,j} - \psi_{i,j}) - r^\alpha_{i-1/2,j}(\psi_{i,j} - \psi_{i-1,j})) + (\psi_{i,j+1} - 2\psi_{i,j} + \psi_{i,j-1})/\delta z^2$$
$$= \frac{1}{r^\alpha_{i,j}\delta r}(r^\alpha_{i+1/2,j}\tilde{u}_{i+1/2,j} - r^\alpha_{i-1/2,j}\tilde{u}_{i-1/2,j}) + (\tilde{v}_{i,j+1/2} - \tilde{v}_{i,j-/12})/\delta z \tag{36}$$

• *k-Equation*

$$k^{k+1}_{i,j} = k^k_{i,j} + \delta t \left\{ \mathrm{CONV}(k)|_{i,j} + \frac{1}{Re\, r^\alpha_{i,j}\delta r^2} [r^\alpha_{i+1/2,j}(1 + (v_{ti+1,j} + v_{ti,j})/2\sigma_k)(k_{i+1,j} - k_{i,j}) \right.$$
$$- r^\alpha_{i-1/2,j}(1 + (v_{ti,j} + v_{ti-1,j})/2\sigma_k)(k_{i,j} - k_{i-1,j})]$$
$$+ \frac{1}{Re\,\delta z^2} [(1 + (v_{ti,j+1} + v_{ti,j})/2\sigma_k)(k_{i,j+1} - k_{i,j})$$
$$\left. - (1 + (v_{ti,j} + v_{ti,j-1})/2\sigma_k)(k_{i,j} - k_{i,j-1})] + P_{i,j} - \varepsilon_{i,j} \right\}^k \tag{37}$$

Copyright © 2004 John Wiley & Sons, Ltd.

where

$$\mathrm{CONV}(k)|_{i,j}^{k} = \left[\frac{1}{r^{\alpha}}\frac{\partial(r^{\alpha}uk)}{\partial r} + \frac{\partial(vk)}{\partial z}\right]\Bigg|_{i,j}^{k} \tag{38}$$

- *ε-Equation*

$$\begin{aligned}\varepsilon_{i,j}^{k+1} = \varepsilon_{i,j}^{k} + \delta t \Bigg\{ & \mathrm{CONV}(\varepsilon)|_{i,j} + \frac{1}{Re\, r_{i,j}^{\alpha}\delta r^{2}}[r_{i+1/2,j}^{\alpha}(1+(v_{ti+1,j}+v_{ti,j})/2\sigma_{\varepsilon})(\varepsilon_{i+1,j}-\varepsilon_{i,j}) \\ & - r_{i-1/2,j}^{\alpha}(1+(v_{ti,j}+v_{ti-1,j})/2\sigma_{\varepsilon})(\varepsilon_{i,j}-\varepsilon_{i-1,j})] \\ & + \frac{1}{Re\,\delta z^{2}}[(1+(v_{ti,j+1}+v_{ti,j})/2\sigma_{\varepsilon})(\varepsilon_{i,j+1}-\varepsilon_{i,j}) \\ & - (1+(v_{ti,j}+v_{ti,j-1})/2\sigma_{\varepsilon})(\varepsilon_{i,j}-\varepsilon_{i,j-1})] + (C_{1\varepsilon}P_{i,j} - C_{2\varepsilon}\varepsilon_{i,j})/T_{ti,j} + \beta E_{i,j} \Bigg\}^{k}\end{aligned} \tag{39}$$

where

$$\mathrm{CONV}(\varepsilon)|_{i,j}^{k} = \left[\frac{1}{r^{\varepsilon}}\frac{\partial(r^{\alpha}u\varepsilon)}{\partial r} + \frac{\partial(v\varepsilon)}{\partial z}\right]\Bigg|_{i,j}^{k} \tag{40}$$

The eddy viscosity, the production of turbulence, the gradient dissipation and the time scale are discretized, respectively, as follows:

$$v_{t\,i,j}^{k} = C_{\mu}f_{\mu}k_{i,j}^{k}T_{ti,j}^{k} \tag{41}$$

$$\begin{aligned}P_{i,j}^{k} = v_{ti,j}^{k}\Bigg\{ & 2\left[\frac{1}{\delta r^{2}}(u_{i+1/2,j}-u_{i-1/2,j})^{2} + \frac{1}{\delta z^{2}}(v_{i,j+1/2}-v_{i,j-1/2})^{2} + \alpha\left(\frac{u_{i+1/2,j}+u_{i-1/2,j}}{2r_{i,j}^{\alpha}}\right)^{2}\right] \\ & + \left[\frac{1}{4\delta z}(u_{i+1/2,j+1}+u_{i-1/2,j+1}-u_{i+1/2,j-1}-u_{i-1/2,j-1})\right. \\ & \left. + \frac{1}{4\delta r}(v_{i+1,j+1/2}+v_{i+1,j-1/2}-v_{i-1,j+1/2}-v_{i-1,j-1/2})\right]^{2}\Bigg\}^{k}\end{aligned} \tag{42}$$

$$\begin{aligned}E_{i,j}^{k} = \frac{2v_{t\,i,j}^{k}}{Re}\Bigg\{ & \frac{1}{4\delta r^{4}}(v_{i+1,j+1/2}+v_{i+1,j-1/2}-2(v_{i,j+1/2}+v_{i,j-1/2})+v_{i-1,j+1/2}+u_{i-1,j-1/2})^{2} \\ & + \frac{1}{4\delta z^{4}}(u_{i+1/2,j+1}+u_{i-1/2,j+1}-2(u_{i+1/2,j}+u_{i-1/2,j})+u_{i+1/2,j-1}+u_{i-1/2,j-1})^{2}\Bigg\}^{k}\end{aligned} \tag{43}$$

Copyright © 2004 John Wiley & Sons, Ltd.

$$T_{ti,j}^{k} = (1-\beta)\,\mathrm{Min}\left\{\frac{k_{i,j}}{\varepsilon_{i,j}}, \frac{2}{3C_\mu}\sqrt{\frac{3}{8(|\mathbf{S}|^2)_{i,j}}}\right\} + \beta\left\{\frac{k_{i,j}}{\varepsilon_{i,j}} + \left(\frac{1}{\varepsilon_{i,j}}\right)^{1/2}\right\}^{k} \tag{44}$$

Note that

$$|\mathbf{S}|^2 = \mathbf{D}:\mathbf{D} = \left(\frac{\partial u}{\partial r}\right)^2 + \left(\frac{\partial v}{\partial z}\right)^2 + \frac{1}{2}\left(\frac{\partial u}{\partial z} + \frac{\partial v}{\partial r}\right)^2$$

and this quantity is discretised as

$$\begin{aligned}(|\mathbf{S}|^2)_{i,j}^{k} = \Bigg\{ & \frac{1}{\delta r^2}\left(u_{i+1/2,j} - u_{i-1/2,j}\right)^2 + \frac{1}{\delta z^2}\left(v_{i,j+1/2} - v_{i,j-1/2}\right)^2 \\ & + \frac{1}{2}\left[\frac{1}{4\delta z}\left(u_{i+1/2,j+1} + u_{i-1/2,j+1} - u_{i-1/2,j-1} - u_{i+1/2,j-1}\right)\right. \\ & \left. + \frac{1}{4\delta r}\left(v_{i+1,j+1/2} + v_{i+1,j-1/2} - v_{i-1,j-1/2} - v_{i-1,j+1/2}\right)\right]^2\Bigg\}^{k}\end{aligned}$$

5.1. Discretization of the convective terms

From now on, a high-order upwinding scheme is used for the discretization of the convective terms in the transport equations (1)–(5). For brevity, only the discretizations of the convective terms (33) and (38) are summarized; all the other convective derivatives are treated similarly (for more details, see Reference [30]). The non-linear derivatives in those terms are approximated by

$$\left.\frac{\partial(r^\alpha uu)}{\partial r}\right|_{i+1/2,j} \approx \left[r_{i+1,j}^{\alpha}(\bar{u}_{i+1,j}u_{i+1,j}) - r_{i,j}^{\alpha}(\bar{u}_{i,j}u_{i,j})\right]/\delta r \tag{45}$$

$$\left.\frac{\partial(uv)}{\partial z}\right|_{i+1/2,j} \approx \left(\bar{v}_{i+1/2,j+1/2}u_{i+1/2,j+1/2} - \bar{v}_{i+1/2,j-1/2}u_{i+1/2,j-1/2}\right)/\delta z \tag{46}$$

$$\left.\frac{\partial(r^\alpha uk)}{\partial r}\right|_{i,j} \approx \left[r_{i+1/2,j}^{\alpha}(\bar{u}_{i+1/2,j}k_{i+1/2,j}) - r_{i-1/2,j}^{\alpha}(\bar{u}_{i-1/2,j}k_{i-1/2,j})\right]/\delta r \tag{47}$$

$$\left.\frac{\partial(vk)}{\partial z}\right|_{i,j} \approx \left(\bar{v}_{i,j+1/2}k_{i,j+1/2} - \bar{v}_{i,j-1/2}k_{i,j-1/2}\right)/\delta z \tag{48}$$

where $\bar{u}_{i-1/2,j}$, $\bar{u}_{i,j}$, $\bar{u}_{i+1/2,j}$, $\bar{u}_{i+1,j}$, $\bar{v}_{i,j-1/2}$, $\bar{v}_{i,j+1/2}$, $\bar{v}_{i+1/2,j+1/2}$ and $\bar{v}_{i+1,j-1/2}$ are the convective velocities (see Reference [11]). In Equations (45)–(48), the transported properties u and k at grid points $(i+1,j)$, (i,j), $(i+\frac{1}{2},j+\frac{1}{2})$, $(i+\frac{1}{2},j-\frac{1}{2})$ and $(i+\frac{1}{2},j)$, $(i-\frac{1}{2},j)$, $(i,j+\frac{1}{2})$, $(i,j-\frac{1}{2})$, respectively, are approximated by using the upwinding VONOS scheme.

Copyright © 2004 John Wiley & Sons, Ltd.

For example, the kinetic energy k at the point $(i+\frac{1}{2},j)$ is approximated by

$$k_{i+1/2,j} \approx (1-S_2)\left\{\begin{array}{l} k_{i,j}, \quad \text{if } \hat{k}_{i,j} \notin [0,1] \\ 10k_{i,j} - 9k_{i-1,j}, \quad \text{if } \hat{k}_{i,j} \in [0,3/74) \\ \frac{3}{8}k_{i+1,j} + \frac{6}{8}k_{i,j} - \frac{1}{8}k_{i-1,j}, \quad \text{if } \hat{k}_{i,j} \in [3/74,1/2) \\ 1.5k_{i,j} - 0.5k_{i-1,j}, \quad \text{if } \hat{k}_{i,j} \in [1/2,2/3) \\ k_{i+1,j}, \quad \text{if } \hat{k}_{i,j} \in [2/3,1] \end{array}\right\}$$

$$+S_2\left\{\begin{array}{l} k_{i+1,j}, \quad \text{if } \hat{k}_{i+1,j} \notin [0,1] \\ 10k_{i+1,j} - 9k_{i+2,j}, \quad \text{if } \hat{k}_{i+1,j} \in [0,3/74) \\ \frac{3}{8}k_{i,j} + \frac{6}{8}k_{i+1,j} - \frac{1}{8}k_{i+2,j}, \quad \text{if } \hat{k}_{i+1,j} \in [3/74,1/2) \\ 1.5k_{i+1,j} - 0.5k_{i+2,j}, \quad \text{if } \hat{k}_{i+1,j} \in [1/2,2/3) \\ k_{i,j}, \quad \text{if } \hat{k}_{i+1,j} \in [2/3,1] \end{array}\right\}$$

where the parameters S_1 and S_2 are given by

$$S_1 = \begin{cases} 0, & \text{if } \bar{u}_{i+1/2,j+1/2} \geqslant 0 \\ 1, & \text{otherwise} \end{cases} \quad \text{and} \quad S_2 = \begin{cases} 0, & \text{if } \bar{u}_{i+1/2,j} \geqslant 0 \\ 1, & \text{otherwise} \end{cases}$$

and the constants $\hat{k}_{i,j}$ and $\hat{k}_{i+1,j}$ are defined as normalized variables (see Reference [38]).

There are of course a number of different high order approaches that have been employed to deal with the convective terms. Our reason for selecting VONOS was that it performed well on a difficult test problem (see Reference [16]) from among an (admittedly non-inclusive) set of possible methods.

It is worth noting that, for physical reasons [39], a desirable property of a difference scheme for k–ε models is positivity. Developing a discretization of the k–ε equations that ensures the positivity of the computed quantities throughout the flow domain and during the course of the iterations is, in general, a difficult task. The non-linear advection scheme employed in this paper has built-in monotonicity, but the other non-linear terms could lead to the possibility of overshoots and undershoots in k and ε, and even artificial negative values. In order to avoid unphysical transient solutions, we set any values of turbulence variables, that are less than zero, to the upstream values.

6. CODE VALIDATION

In this section, we shall present fluid flow problems which will be used to validate the numerical method described in this paper.

Copyright © 2004 John Wiley & Sons, Ltd.

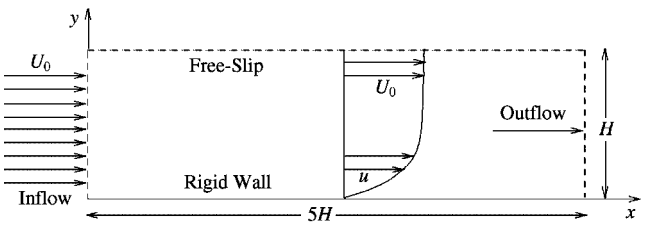

Figure 2. Sketch of the flow field and computational domain: $U_0 = 1.0\,\mathrm{m\,s^{-1}}$ and $H = 1.0\,\mathrm{m}$.

6.1. Turbulent boundary layer over a flat plate

A two dimensional zero-pressure-gradient turbulent boundary layer over a flat plate is first used to validate the numerical technique. This fluid flow problem has frequently appeared in the literature, and several methods have been proposed to estimate the skin-friction coefficient C_f [40]. Figure 2 shows schematically the geometry of the fluid flow problem in Cartesian co-ordinates and the parameters used in the present simulation.

The Reynolds number, based on the inflow velocity U_0 and the channel height H, is $Re = 2.0 \times 10^6$. Computations are performed on three different meshes, namely: the coarse mesh (20×100 computational cells, $\delta x = \delta y = 0.05\,\mathrm{m}$); the medium mesh ($40 \times 200$ computational cells, $\delta x = \delta y = 0.025\,\mathrm{m}$) and the fine mesh ($80 \times 400$ computational cells, $\delta x = \delta y = 0.0125\,\mathrm{m}$). In these simulations, four marker particles per inflow cell were used. In what follows, we present three well-known analytical estimates of the skin-friction coefficient and a numerical estimate obtained by the GENSMAC code equiped with the $H\,Re$ k–ε model.

Figure 3 compares the dimensionless turbulent skin-friction coefficient $C_f = 2\tau_w$ as calculated by GENSMAC using the $H\,Re$ k–ε model with the estimates given by Prandtl, power-law and White (see, for example, Reference [34]). The figures display C_f against the local Reynolds number $Re_x = U_0 x/\nu_0$ at the (non-dimensional) time $t = 6.477$ on three different sized meshes. Additionally, the corresponding laminar result is also included. As shown in Figures 3(a)–(c), the numerical estimates are generally satisfactory for Re_x beyond 1.0×10^6. It can also be observed from Figure 3(d) that when the coarse mesh is twice refined, there appeared to be convergence of the numerical solution to a profile near the power-law and the White profiles. On the other hand, for $Re_x \leqslant 1.0 \times 10^6$, a systematic discrepancy existed and this may be due to the uniform meshes used and/or the initial velocity profile not being sufficiently turbulent at the entrance region.

In order to investigate the performance of the numerical method in regions where the turbulent stress is predominant, we fix the non-dimensional location $x = 3.75$ at the plate and extract the velocity profile $u^+ = u^+(\ln y^+)$ at this point using the numerical solution in the medium sized mesh. This profile was then compared with experimental data from Wieghardt and Tillmann [41] and two profiles derived by varying the constants K and B in the law (25). One of these profiles, proposed by Nikuradse and Prandtl (see, for instance, Reference [34]) assumes the values $K = 0.40$ and $B = 5.50$, and the other, estimated by Coles and Hirst [42], uses the values $K = 0.41$ and $B = 5.00$. Figure 4 presents a comparison of these two profiles and some experimental data with the computed profile. The results display a degree of compatibility suggesting that the effective stress tensor estimated at the wall

Copyright © 2004 John Wiley & Sons, Ltd.

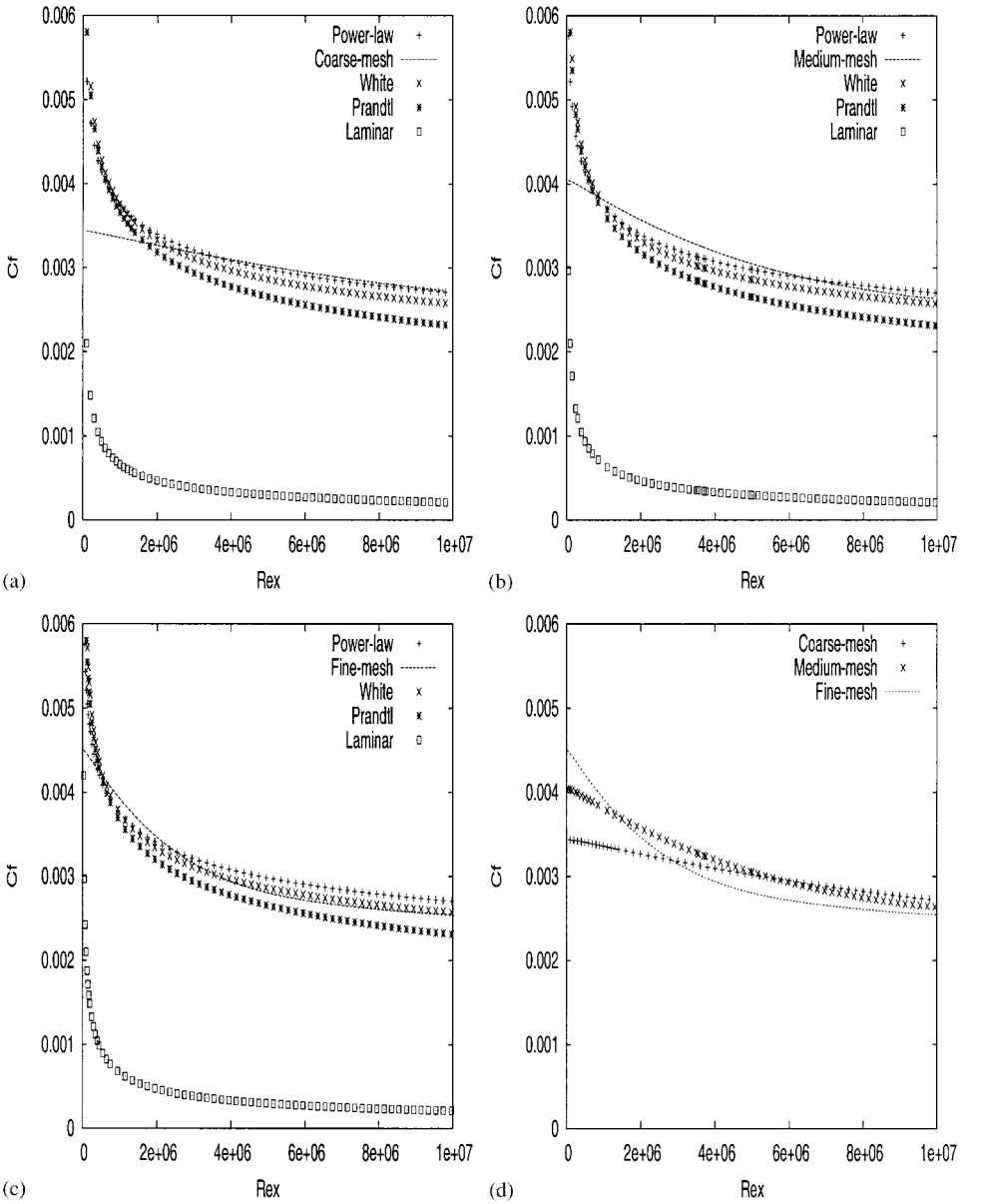

Figure 3. Comparison between the skin-friction coefficient profiles $C_f = C_f(Re_x)$ for the turbulent boundary layer on a flat plate calculated using the *H Re* k–ε model and theoretical estimates: (a) comparison in the coarse mesh; (b) comparison in the medium mesh; (c) comparison in the fine mesh and (d) comparison of the three numerical solutions.

is providing the correct condition for the solution in the region with $z^+ > 500$. Thus, the numerical solution of the *H Re* k–ε model is a reasonable simulation of turbulence in regions remote from the rigid boundary.

Copyright © 2004 John Wiley & Sons, Ltd.

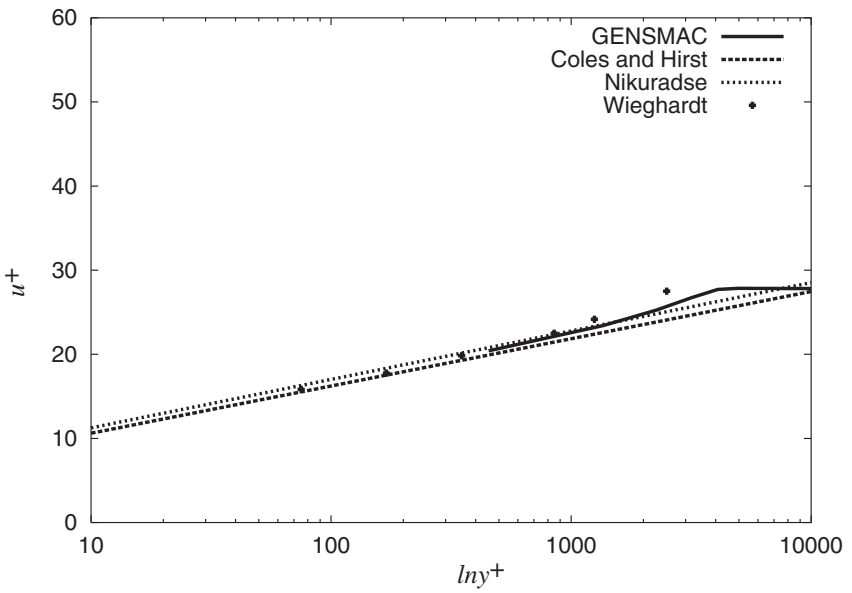

Figure 4. A comparison between the numerical solution of the velocity in the turbulent boundary layer and (a) profile given by Coles and Hirst; (b) profile given by Nikuradse and (c) experimental data given by Wieghardt and Tillmann.

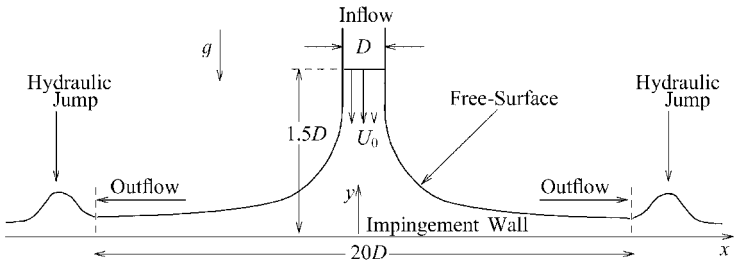

Figure 5. Schematic of the physical problem, showing the geometry and parameters: $U_0 = 1.0\ \mathrm{m\ s^{-1}}$ and $D = 0.010\ \mathrm{m}$.

6.2. *Turbulent planar jet impinging on a flat surface*

The $H\,Re$ k–ε and $L\,Re$ k–ε models will now be employed to solve a planar jet impinging onto a flat surface. The geometry and parameters are schematically represented in Figure 5. For this free surface fluid flow problem, the Reynolds number based on the inflow velocity U_0 and inflow diameter D is $Re = 1.6 \times 10^4$, and the Froude number is $Fr = U_0/\sqrt{gD} = 3.193$. Three different meshes will be used, namely: the coarse mesh (25×50 computational cells, $\delta x = \delta y = 0.002\,\mathrm{m}$); the medium mesh ($50 \times 200$ computational cells, $\delta x = \delta y = 0.001\,\mathrm{m}$); and the fine mesh ($100 \times 400$ computational cells, $\delta x = \delta y = 0.0005\ \mathrm{m}$). In these computations,

Copyright © 2004 John Wiley & Sons, Ltd.

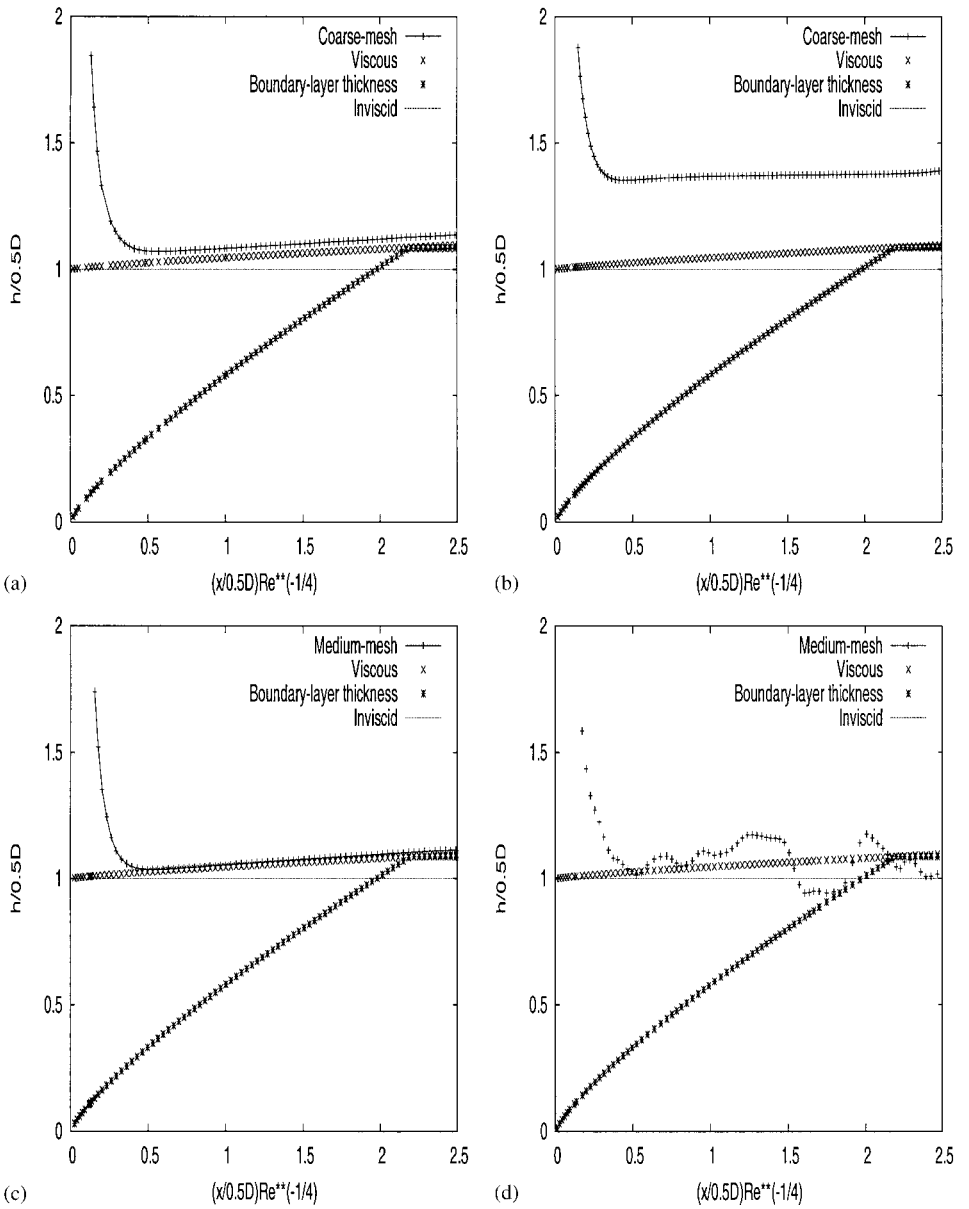

Figure 6. Comparison between the free surface height obtained by two dimensional $H\,Re$ k–ε (left column) and $L\,Re$ k–ε (right column) models and approximate analytical solutions by Watson.

three marker particles per inflow cell were used. In the following, a quantitative comparison will be performed in order to compare Watson's two-dimensional analytical predictions for turbulent flow [43] with the numerical results. Figure 6 plots the non-dimensional free surface height $h/0.5D$ against the non-dimensional distance $(x/0.5D)Re^{-1/4}$. The numerical results

Copyright © 2004 John Wiley & Sons, Ltd.

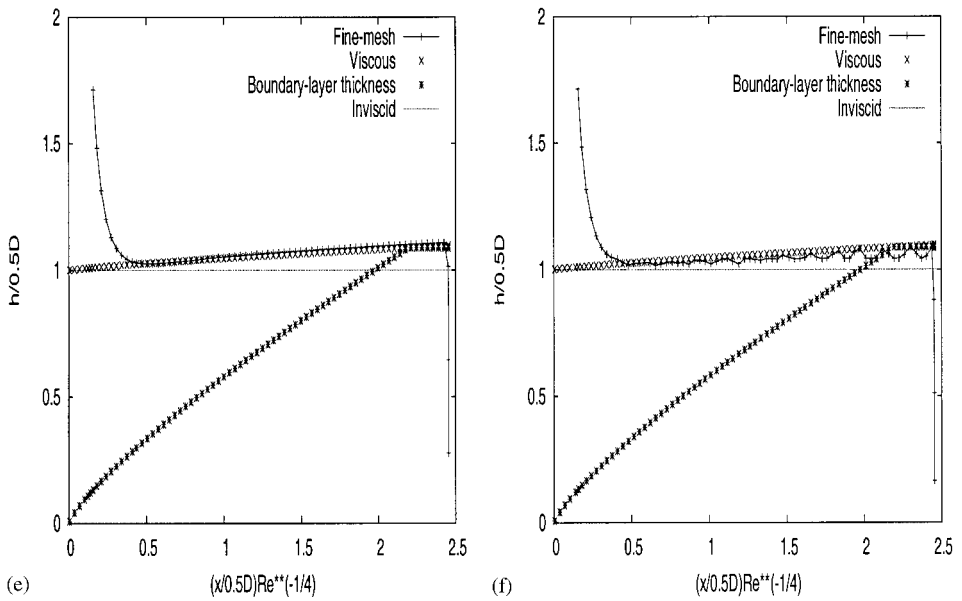

Figure 6. *Continued.*

were obtained by solving the $H\,Re$ k–ε model (Figures 6(a), (c) and (e)—left column) and $L\,Re$ k–ε model (Figures 6(b), (d) and (f)—right column) for three different sized meshes. The computations were given at the non-dimensional time $t = 38.0$ and a comparison with the inviscid and viscous solutions of Watson [43] was effected. Additionally, we have also included Watson's boundary layer thickness. It can be seen, from Figure 6 (left column) and Figure 7(a), that the calculations using the $H\,Re$ k–ε model on fine mesh (200×400 grid points) provide practically the same results as those obtained on the coarse and medium meshes, indicating grid independence of the numerical results. One can note also that the numerical results on the coarse and medium meshes monotonically converge to the numerical solution on the fine mesh, and that the numerical solution on the fine mesh is in good agreement with the Watson's viscous solution.

A comparison between the free surface height obtained from the $L\,Re$ k–ε model and the Watson's viscous solution was also made, and the results are displayed in the Figure 6 (right column) and Figure 7(b). These were computed at the same non-dimensional time, as for the $H\,Re$ k–ε model. It is obvious that the numerical results with this turbulence model on the three meshes are unsatisfactory. We believe that for this specific fluid flow problem the disagreement between the viscous analytical solution, developed by Watson, and the numerical solution, obtained by using the $L\,Re$ $k - \varepsilon$ model, may be attributed to the fact that the numerical solution has been calculated on a uniform mesh resulting in a poor resolution of the viscous sublayer. In fact, for flow dynamics at this Reynolds number the thickness of the viscous sublayer of the turbulent boundary layer is so thin ($O(\nu/u_\tau)$) that it would be difficult to resolve it in any reasonable time.

The performance of the numerical methods in the calculation of the mean velocity and eddy viscosity was also assessed, and comparisons, using the fine mesh between the non-dimensional

Copyright © 2004 John Wiley & Sons, Ltd.

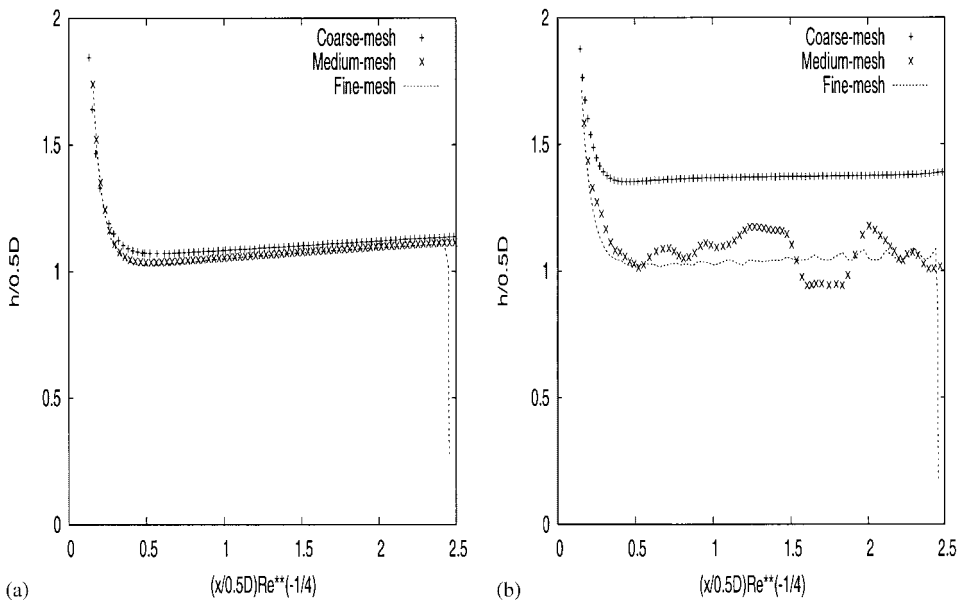

Figure 7. Comparison between the three numerical solutions: (a) *H Re* k–ε model and (b) *L Re* k–ε model.

numerical solution obtained from the *H Re* k–ε model and non-dimensional analytic solutions derived by Watson are presented in Figure 8. The first two plots, parts (a) and (b), of this figure represent, respectively, the x-component of the mean velocity, u and the eddy viscosity, ν_t, along the horizontal station $y/D = 0.00025$. The next plot, part (c), compares numerical and analytical profiles for u along the vertical station $x/D = 19.675$. Part (d) of the figure shows the numerical and analytical profiles for u along the free surface. It is seen from this figure that the agreement between the computed results with *H Re* $k-\varepsilon$ model and analytical results can be said to be satisfactory. With the *L Re* k–ε model, once more, the agreement is much less satisfactory (not shown). It should also be observed that the success in capturing mean velocity and turbulent quantities depends rather crucially on the grid resolution and the turbulence modelling.

6.3. Turbulent axisymmetric jet impinging on a flat surface

In this subsection, both the *H Re* k–ε and *L Re* k–ε models will be studied for an axisymmetric jet impinging onto a flat surface. Figure 9 shows the geometry of the problem and the parameters used in the present computation.

For this problem, the Reynolds number based on the inflow velocity U_0 and inflow diameter D is $Re = (\pi/2)U_0 D/\nu = 5.03 \times 10^4$, and the Froude number is $Fr = U_0/\sqrt{gD} = 2.26$. For this free surface flow, three different meshes were also used and will be referred to as the coarse mesh (50×100 computational cells, $\delta r = \delta z = 0.001$ m), the medium mesh (100×200 computational cells, $\delta r = \delta z = 0.0005$ m), and the fine mesh (200×400 computational cells, $\delta r = \delta z = 0.00025$ m). In these computations, three marker particles per inflow cell were used.

Copyright © 2004 John Wiley & Sons, Ltd.

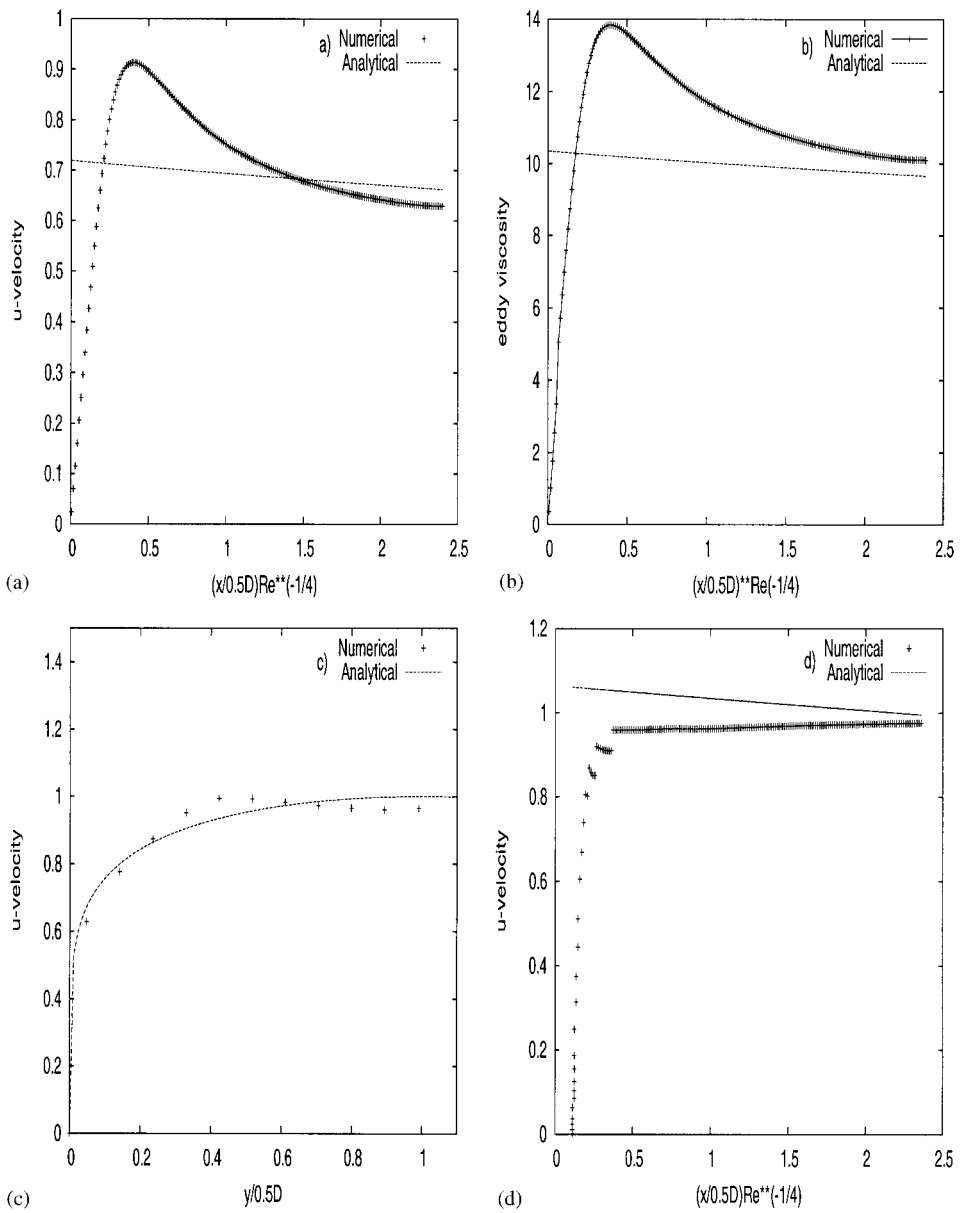

Figure 8. Comparison between numerical and analytical results: (a) and (b) mean velocity and eddy-viscosity profiles at station $y/D = 0.00025$; (c) mean velocity profiles at station $x/D = 19.675$ and (d) mean velocity profiles at the free surface.

A quantitative comparison between Watson's axisymmetric analytical predictions [43] and the numerical results will now be performed. Figure 10 displays a comparison between the variation of the non-dimensional free surface height $(h/0.5D)Re^{1/9}$ with non-dimensional

Copyright © 2004 John Wiley & Sons, Ltd.

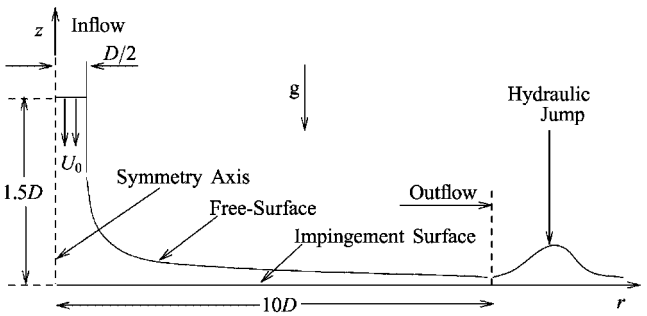

Figure 9. Configuration of the flow field, showing geometry and parameters: $U_0 = 2.0\ \mathrm{m\ s^{-1}}$ and $D = 0.10$ m.

distance $(r/0.5D)Re^{-1/9}$. The numerical results were obtained by solving the *H Re* k–ε model (Figures 10(a), (c) and (e)—left column) and *L Re* k–ε model (Figures 10(b), (d) and (f)—right column) on the three meshes. The computations were given at the non-dimensional time $t = 20.48$, along with the approximate viscous and inviscid axisymmetric solutions of Watson [43]. It can be seen, from the left column of this set of figures, that the numerical solutions using the *H Re* k–ε model on coarse and medium meshes monotonically converge to the numerical solution on the fine mesh and the numerical solution on the fine mesh shows reasonable agreement with Watson's turbulent viscous solution. A comparison between the surface height obtained from the *L Re* k–ε model and Watson's viscous solution was also made at the same non-dimensional time, and the results are displayed in the right hand column of the Figure 10. It is clear that the numerical results with this turbulence model on the coarse and medium meshes were unsatisfactory, whereas the fine mesh provides a solution near Watson's viscous solution.

As in the previous calculations, a possible explanation for the discrepancy between the viscous analytical solution developed by Watson and the numerical solution obtained by the *L Re* k–ε model might be attributed to the poor resolution of the viscous sublayer. On the other hand, the discrepancy between the viscous solution of Watson and the *H Re* k–ε model may be due to the assumptions Watson had to make in order to obtain his analytical solutions. Indeed, Watson himself points out a discrepancy between his turbulent viscous solution and experimental data.

7. APPLICATIONS

We conclude this paper by presenting numerical simulations of free surface turbulent flows using the *H Re* k–ε model. The problems consist of a horizontal jet penetrating a quiescent fluid from an entry port at various depths, denoted by H, beneath the free surface. The geometrical configuration, as well as the parameters employed, for this free surface fluid flow is shown in Figure 11. In this computation, the associated Reynolds and Froude numbers are $Re = DU_0/\nu = 5.0 \times 10^4$ and $Fr = U_0/\sqrt{gD} \approx 1.8$, respectively. Also, for all runs, the number of marker particles per inflow and full cells is three.

Copyright © 2004 John Wiley & Sons, Ltd.

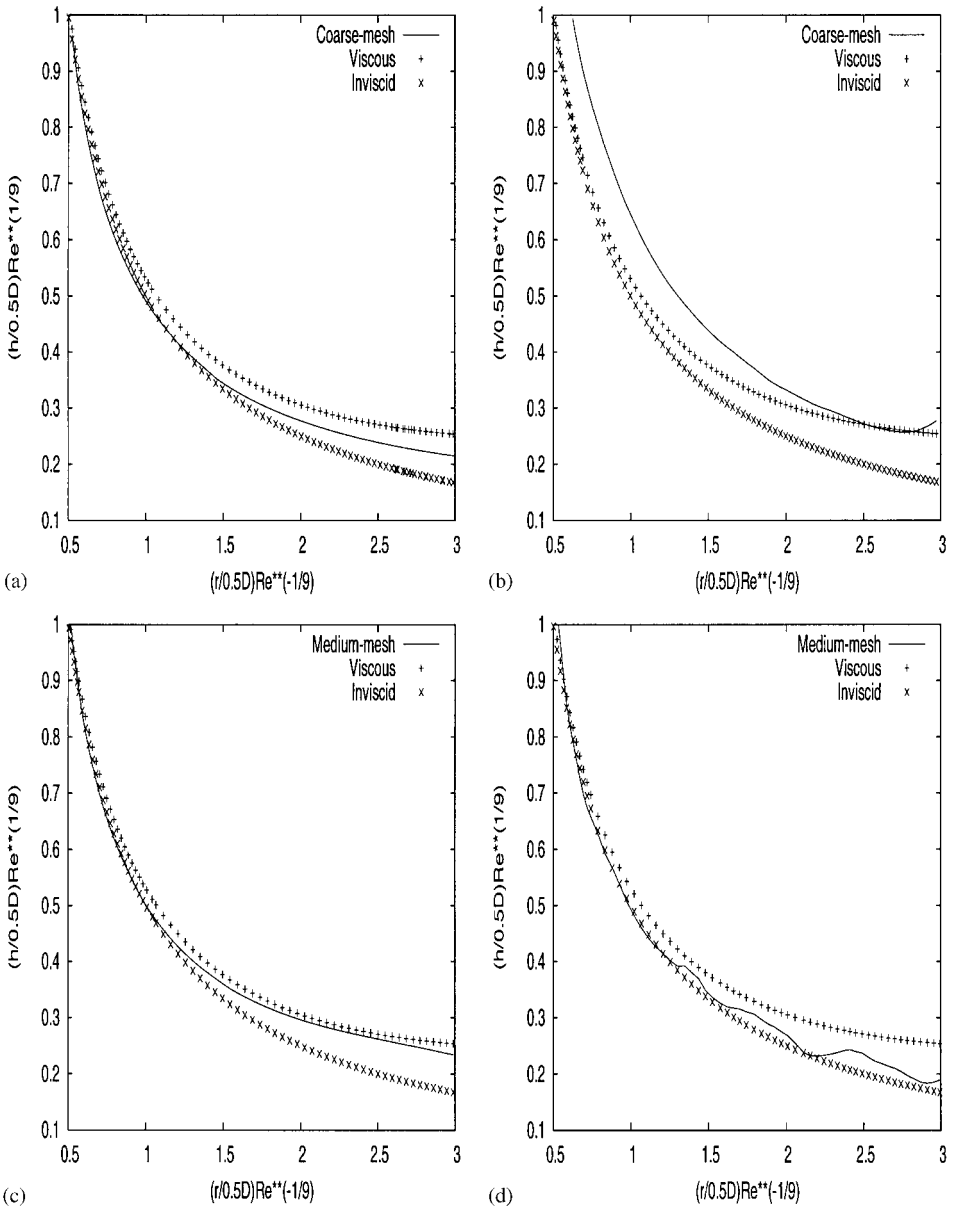

Figure 10. Comparison between the free surface height obtained by the axisymmetric $H\,Re$ k–ε (left column) and $L\,Re$ k–ε (right column) models and approximate analytical solutions of Watson.

The numerical simulations of the free surface fluid flow problem described above are performed for three cases, namely: $H = 6.0$, 1.0 and 0.5 m. The development of non-dimensional vorticity distributions, together with the free surface elevation at various non-dimensional times are presented in Plates 1 through 3.

Copyright © 2004 John Wiley & Sons, Ltd.

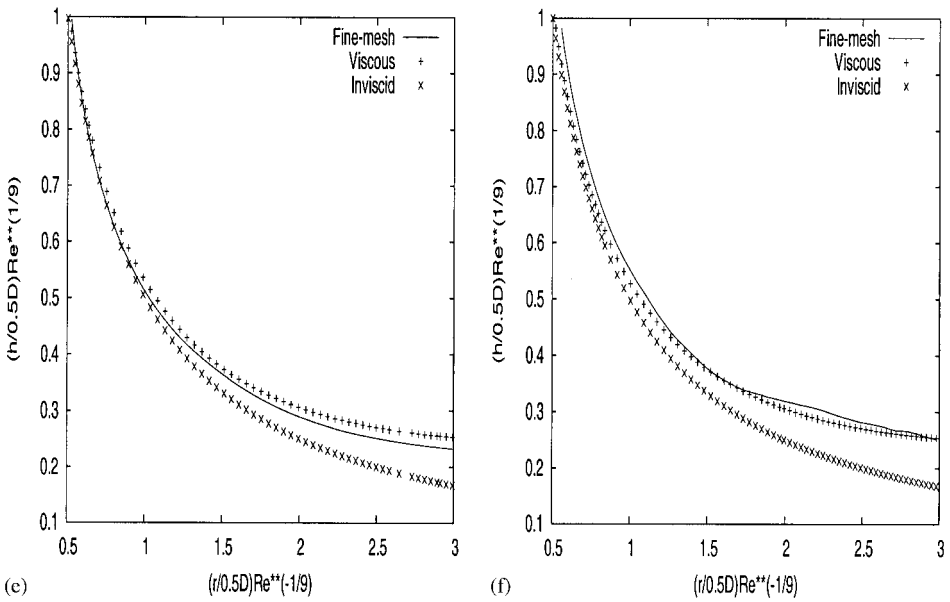

Figure 10. *Continued*

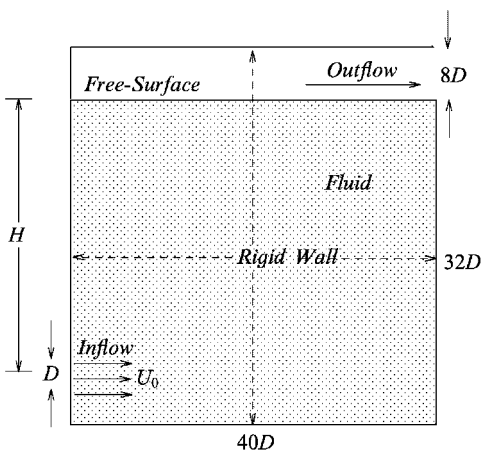

Figure 11. Geometry and parameters for the free surface fluid flow of a penetrating planar jet in a pool: $U_0 = 2.0\ \mathrm{m\,s^{-1}}$ and $D = 0.25$ m.

Plate 1 depicts the case $H = 6.0$ m, which corresponds to the entry port far from the free surface. In this case, the interaction with the free surface occurs only at the later stages of the flow development. Initially, one can observe the growth of the instability of the boundary layers between the entering jet and the stagnant fluid and, subsequently, the formation of a pair

Copyright © 2004 John Wiley & Sons, Ltd.

of counter-rotating eddies. Later on, at non-dimensional time $t = 67.2$, the first pair of eddies propagates towards the free surface. As these eddies reach the free surface, at non-dimensional time $t = 105.6$, they start to move parallel to it, one to the left and one to the right. At this time it is also possible to notice the characteristic signature of an upwelling vortex pair, which is given by an elevated central part, corresponding to the region between the vortices; two depressions can be observed on the far side of each vortex. From the interaction of these two eddies two smaller eddies begin to form in the region of the depressions creating two new pairs of eddies. At non-dimensional time $t = 121.6$, the new eddies are strong enough to induce a downward velocity and to cause the eddies to separate from the surface. In the meanwhile, in the region close to the jet entrance, other vortical structures undergo pairing interactions producing larger vortical structures as the jet penetrates the pool.

In the second simulation (Plate 2, with $H = 1.0$ m) the jet emerges quite close to the surface, and the flow begins to interact with the free surface at an early stage. Some fluid is entrained by the jet from the surface. The start-up vortex pair propagates both outwards and towards the bottom of the pool, describing a large circular arc. Meanwhile, other vortex pairs are generated close to the injection position. As its size increases, the upper vortex interacts with the free surface causing an upwelling at the free surface. The upwelling increases as the vortex is pushed upward by other smaller vortex of opposite rotation. At later stages, the magnitude of the non-dimensional vorticity is reduced, we believe, by a build up of the turbulent eddy viscosity.

The third case ($H = 0.5$ m), shown in Plate 3, corresponds to a shallow jet that has a strong interaction with the free surface. From the beginning, the vortices interact with the free surface causing the formation of undulations on the free surface. As time progresses, the undulations become more intense until, at later times, the strengths of the vorticities decrease dramatically away from the injection point causing a reduction in the surface roughness. In Figure 12 more information is provided about the non-dimensional distributions of calculated mean velocities and mean values of turbulence quantities at the non-dimensional time $t = 52$, in addition to the fluid flow structure at the free surface at the non-dimensional time $t = 33.6$.

These simulations produce results that are consistent with previous simulations and/or experiments [44], and we believe may be regarded as quite realistic. Similar vortical structures have been reported for jets issued in confined domains without free surfaces, both for laminar and turbulent flows. In particular, Hirsa and Willmarth [45] and Sarpkaya and Suthon [46] report on the formation of slight surface deformations, called scars. These deformations are caused by vortices of opposite rotation and the respective secondary vortices generated by their interaction with the free surface.

The flow obtained in these simulations is an unsteady flow with some small scale structures, particularly in the last case (see Plate 3 and Figure 12), in which the effect of the free surface is larger. Large eddy simulations of turbulence are simulations in which the energy-containing scales are resolved down to the inertial range which really requires unsteady three-dimensional simulations [47]. The smallest resolved scales in the current simulations are a great deal larger than the turbulent scales (which in any case are associated with the three-dimensional motion) and so it would be inappropriate to consider these simulations as LES approximations. The results of this paper (in particular Figure 12 and Plates 1–3) should be interpreted as representing the two-dimensional motion of one realisation occurring at scales greater than the discretization scale. In other words, both the free surface position and the

Copyright © 2004 John Wiley & Sons, Ltd.

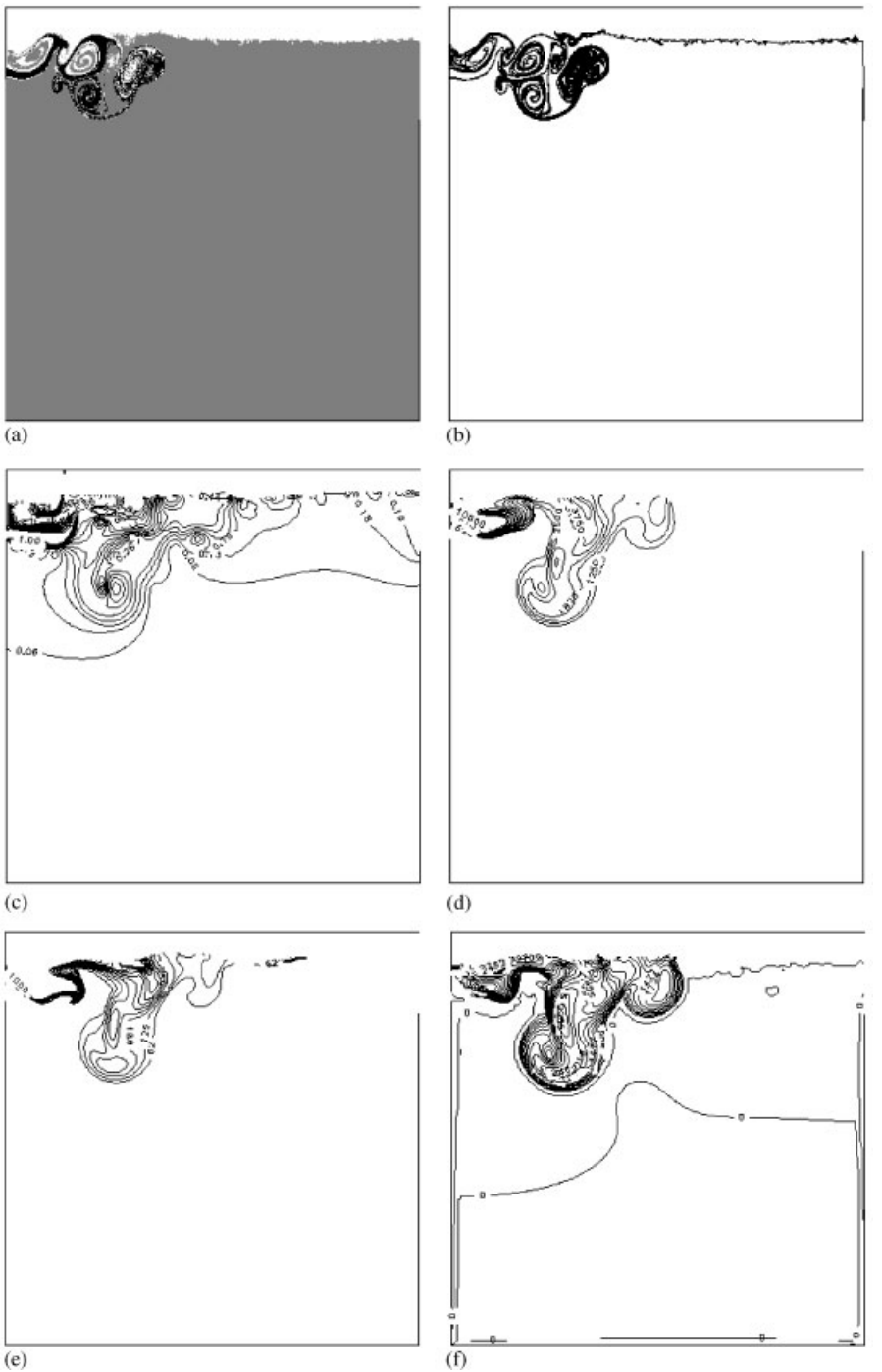

Figure 12. Jet in a pool at non-dimensional time $t = 52$ (case $H = 0.5$ m) showing: (a) filled surface, and (b) flow surface at non-dimensional time $t = 33.6$; (c) mean velocity contours, (d) kinetic energy contours, (e) turbulence dissipation rate contours and (f) eddy viscosity contours.

Copyright © 2004 John Wiley & Sons, Ltd.

velocity fields computed here may be regarded as the deterministic motion at these larger scales. Indeed, these simulations may be thought as time-dependent Reynolds averaged Navier–Stokes (T-RANS) or as very large eddy simulations (VLES) [48], as opposed to the three-dimensional, and much more expensive, LES.

Turbulent flow simulations using LES and DNS approaches have been performed by other authors, but are mostly restricted to very low (or negligible) Froude numbers (see References [49, 50]). The ability to perform simulations for high values of the Froude number is a distinct advantage of the present numerical method.

8. CONCLUSION

This paper has been concerned with adapting the classical front-tracking Marker-and-Cell (MAC) approach to a two-dimensional (and axisymmetric) variant of the k–ε turbulence model. This adaptation was not straightforward and really depended upon building recent work of the authors and, in particular, the GENSMAC code—a modernised version of the MAC approach. In order to achieve an accurate discretisation of the non-linear terms, a second/third-order upwinding technique was required. The closure of the time-averaged Navier–Stokes equations was achieved by using the two-equation eddy-viscosity model: the high Reynolds k–ε model with a time scale proposed by Durbin [19]; and low-Reynolds number form of the k–ε model following Yang and Shih [14].

The code was validated by considering three problems: turbulent boundary layer flow over a flat plate; turbulent planar jet impinging on a flat surface and turbulent axisymmetric jet impinging on a flat surface. The first problem has appeared frequently in the literature and we calculated both the skin friction and the velocity profile, which were then shown to compare favourably with existing experimental data. For the turbulent jet problems results were compared with the approximate analytic results of Watson [43]. For the *H Re* k–ε model the results compared favourably; for *L Re* k–ε model the results were less favourably, but this may be due to the fact that there are discrepancies between Watson's analytic solutions and existing experimental data.

Finally the *H Re* k–ε model was employed to solve the problem of a horizontal jet penetrating a quiescent fluid from an entry port at various depths beneath the free surface. The time evolution of the vorticity contours were displayed for entry points at different heights showing the interaction with the free surface. In addition, the undulations at the free surface, the mean velocity contours, the kinetic energy contours, the turbulence dissipation rate contours and the eddy viscosity contours were all displayed; physical explanations were provided, and the work was placed in context with the existing literature.

In general it may be concluded that the simulations of the *H Re* k–ε model were good, but those for the *L Re* k–ε model were less satisfactory. One advantage of the methodology of this paper is its ability to handle high Froude numbers. Computationaly, it may be speeded up (by up to a factor of 3) by using wall functions.

We believe that these results could be improved by incorporating more physics into the model. With this in mind the authors are considering adaptations fo the renormalization group method (RNG) and the realizable k–ε model.

Copyright © 2004 John Wiley & Sons, Ltd.

ACKNOWLEDGEMENTS

We gratefully acknowledge the support given by Fundação de Amparo à Pesquisa do Estado de São Paulo (*FAPESP*) Contract No. 00/03385-0 and Conselho Nacional de Desenvolvimento Científico e Tecnológico (*CNPq*). We are also grateful to the referees for their useful comments to improve the paper.

REFERENCES

1. Ferziger JH. Simulation of incompressible turbulent flows. *Journal of Computational Physics* 1987; **69**:1–48.
2. Melville WK. The role of surface-wave breaking in air-sea interaction. *Annual Review of Fluid Mechanics* 1996; **28**:279–323.
3. Sarpkaya T. Vorticity, free-surface and surfactants. *Annual Review of Fluid Mechanics* 1986; **28**:88–128.
4. Tsai W-T, Yue DKP. Computations of nonlinear free-surface flows. *Annual Review of Fluid Mechanics* 1996; **28**:249–278.
5. Borue V, Orszag SA, Staroselsky I. Interaction of surface waves with turbulence: direct numerical simulations of turbulent open-channel flow. *Journal of Fluid Mechanics* 1995; **286**:1–23.
6. Pan Y, Banerjee S. A numerical study of free surface turbulence in channel flow. *The Physics of Fluids* 1995; **7**:1649–1664.
7. Tsai W-T. A numerical study of the evolution and structure of a turbulent shear layer under a free surface. *Journal of Fluid Mechanics* 1998; **354**:239–276.
8. Brocchini M, Peregrine DH. The dynamics of strong turbulence at free surfaces. Part 1. Description. *Journal of Fluid Mechanics* 2001; **449**:225–254.
9. Brocchini M, Peregrine DH. The dynamics of strong turbulence at free surfaces. Part 2. Free surface boundary conditions. *Journal of Fluid Mechanics* 2001; **449**:255–290.
10. Walker DT. On the origin of the 'surface current' in turbulent free-surface flows. *Journal of Fluid Mechanics* 1997; **339**:275–285.
11. Shen L, Zhang X, Yue DKP, Triantafyllou GS. The surface layers for free-surface turbulent flows. *Journal of Fluid Mechanics* 1999; **386**:167–212.
12. Launder BE, Spalding DB. The numerical computation of turbulent flows. *International Journal for Numerical Methods in Fluids* 1974; **15**:127–146.
13. Rodi W. *Turbulence models and their applications in hydraulics*. International Association of Hydraulic Research, Delft, the Netherlands, Monografy, 1980.
14. Yang Z, Shih H. New time scale based k–ε model for near-wall turbulence. *AIAA Journal* 1993; **7**:1191–1198.
15. Welch JE, Harlow FH, Shannon JP, Daly BJ. The MAC method. *Los Alamos Scientific Laboratory Report LA-3425*, 1965.
16. Ferreira VG, Tomé MF, Mangiavacchi N, Castelo A, Cuminato JA, Fortuna AO, McKee S. High order upwinding and the hydraulic jump. *International Journal for Numerical Methods in Fluids* 2002; **39**:549–583.
17. Varonos A, Bergeles G. Development and assessment of a variable-order non-oscillatory scheme for convection term discretization. *International Journal for Numerical Methods in Fluids* 1998; **26**:1–16.
18. Tomé MF, McKee S. GENSMAC: a computational marker-and-cell method for free surface flows in general domains. *Journal of Computational Physics* 1994; **110**:171–186.
19. Durbin PA. On the k–ε stagnation point anomaly. *Journal of Heat and Fluid Flow* 1996; **17**:89–90.
20. Hoffman G. Improved form of the low Reynolds number k–ε turbulence model. *The Physics of Fluids* 1975; **18**:309–312.
21. Tomé MF, Castelo A, Murakami J, Cuminato JA, Minghim R, Oliveira CF, Mangiavacchi N, McKee S. Numerical simulation of axisymmetric free surface flows. *Journal of Computational Physics* 2000; **157**: 441–472.
22. Costa JJ, Oliveira LA, Blay D. Test of several versions for the k–ε type turbulence modelling of internal mixed convection flows. *International Journal of Heat and Mass Transfer* 1999; **42**:4391–4409.
23. Wilcox DC. *Turbulence modeling for CFD*, *DCW Industries*, Inc., California, 1993.
24. Nagano Y, Tagawa M. An improved $k-\varepsilon$ model for boundary layer flow. *Transaction of the ASME Journal of Fluids Enginnering* 1990; **112**:33–39.
25. Amano RS, Brandt H. Numerical study of turbulent axisymmetric jets impinging on a flat plate and flowing into an axisymmetric cavity. *Transaction of the ASME Journal on Fluids Engineering* 1984; **106**:410–417.
26. Landau LD, Lifshitz EM. *Fluid mechanics*. Course of Theoretical Plysics, vol. 6. Butterworth-Heinemann: Great Britain, 1975.
27. Sondak DL, Pletcher RH. Application of wall functions to generalized nonorthogonal curvilinear coordinate systems. *AIAA Journal* 1995; **33**:33–41.
28. Patel VC. Perspective: flow at high Reynolds number and over rough surfaces—Achilles Heel of CFD. *Transaction of the ASME Journal on Fluids Enginnering* 1998; **120**:434–444.

Copyright © 2004 John Wiley & Sons, Ltd.

29. Norris HL, Reynolds WC. Turbulent channel flow with a moving wavy boundary. *Stanford Univ. Dept. Mech. Eng. TR TF-7*, 1975.
30. Ferreira VG. Análise e implementação de esquemas de convecção e modelos de turbulência para simulação de escoamentos incompressíveis envolvendo superfícies livres. *Ph.D. Thesis* (www.teses.usp.br), Department of Computer Science and Statistics, USP—University of São Paulo, São Carlos, Brazil, 2001.
31. Merci B, De Langhe C, Vierendeels J, Dick E. A quasi-realizable cubic low-reynolds eddy-viscosity turbulence model with a new dissipation rate equation. *Flow, Turbulence and Combustion* 2001; **66**:133–157.
32. Bradshaw P. *Turbulence*. In *Topics in Applied Physics*, vol. 12. Springer: Berlin, 1976.
33. Wilcox DC. Reassessment of the scale-determining squation for advanced turbulence models. *AIAA Journal* 1988; **26**:1299–1310.
34. White FM. *Viscous Fluid Flow*. McGraw-Hill: New York, 1991.
35. Benim AC, Zinser W. Investigation into the finite element analysis of condined turbulent flows using a $k-\varepsilon$ model of turbulence. *Computer Methods in Applied Mechanics and Engineering* 1985; **51**:507–523.
36. Amsden AA, Harlow FH. A numerical technique for calculating incompressible fluid flow. *Los Alamos Scientific Laboratory Report LA-4370*, 1971.
37. Gaskell PH, Lau AKC. Curvature-compensated convective transport: SMART, a new boundedness-preserving transport algorithm. *International Journal for Numerical Methods in Fluids* 1988; **8**:617–641.
38. Leonard BP. Simple high-accuracy resolution program for convective modelling of discontinuities. *International Journal for Numerical Methods in Fluids* 1988; **8**:1291–1318.
39. Zijlema M, Segal A, Wesseling P. Invariant discretization of the $k-\varepsilon$ model in general co-ordinates for prediction of turbulent flow in complicated geometries. *Computers and Fluids* 1995; **24**:209–225.
40. Ferziger JH, Lyrio AA, Bardina JG. New skin friction and entrainment correlations for turbulent boundary layers. *Transaction of the ASME Journal on Fluids Enginnering* 1982; **104**:407–544.
41. Wieghardt K, Tillmann W. On the turbulent friction layer for rising pressure. *NACA Technical Memo. 1314*, 1951.
42. Coles DE, Hirst EA. Computation of turbulent boundary layer. *AFOSRIFFP Stanford Conference*, *Proceedings of Conference*, vol. 2. Stanford University, 1968.
43. Watson EJ. The radial spread of a liquid jet over a horizontal plane. *Journal of Fluid Mechanics* 1964; **20**: 481–499.
44. Walker DT, Leighton RI, Garza-Rios LO. Shear-free turbulence near a flat free surface. *Journal of Fluid Mechanics* 1996; **320**:19–51.
45. Hirsa A, Willmarth WW. Measurements of vortex pair interaction with a clean or contaminated free-surface. *Journal of Fluid Mechanics* 1994; **259**:25–45.
46. Sarpkaya T, Suthon P. Interaction of a vortex couple with a free-surface. *Experiments in Fluids* 1991; **11**: 205–217.
47. Lesieur M, Métais O. New trends in large eddy simulations of turbulence. *Annual Review of Fluid Mechanics* 1996; **28**:45–82.
48. Speziale CG. Turbulence modeling for time-dependent RANS and VLES: a review. *AIAA Journal* 1998; **36**:173–184.
49. Mangiavacchi N, Gundlapalli R, Akhavan R. Dynamics of a turbulent jet interacting with a free surface. *ASME Symposium on Free Surface Turbulence*, Lake Tahoe, NV, USA, 1994.
50. Shen L, Yue DKP. Large-eddy simulation of free-surface turbulence. *Journal of Fluid Mechanics* 2001; **440**: 75–116.
51. Rockwell D, Lin JC, Cetiner O, Downes K, Yang Y. Quantitative imaging of the wake of a cylinder in a steady current and free-surface waves. *Journal of Fluids and Structures* 2001; **15**:427–443.

Copyright © 2004 John Wiley & Sons, Ltd.

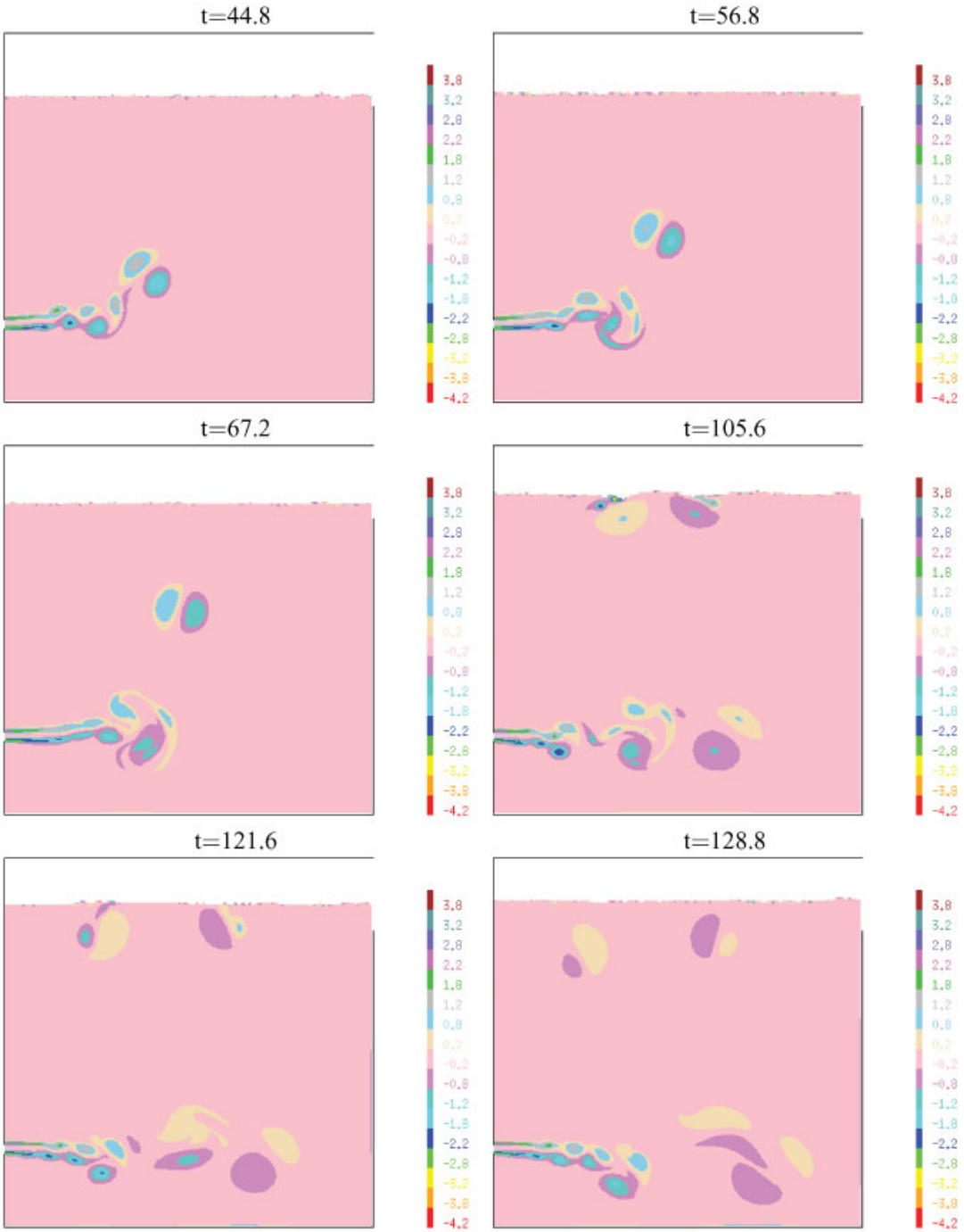

Plate 1. Non-dimensional time evolution of the non-dimensional vorticity contours of a two-dimensional numerical simulation, using the $H\,Re$ k–ε model. $H = 6.0$ m.

Copyright © 2004 John Wiley & Sons, Ltd.

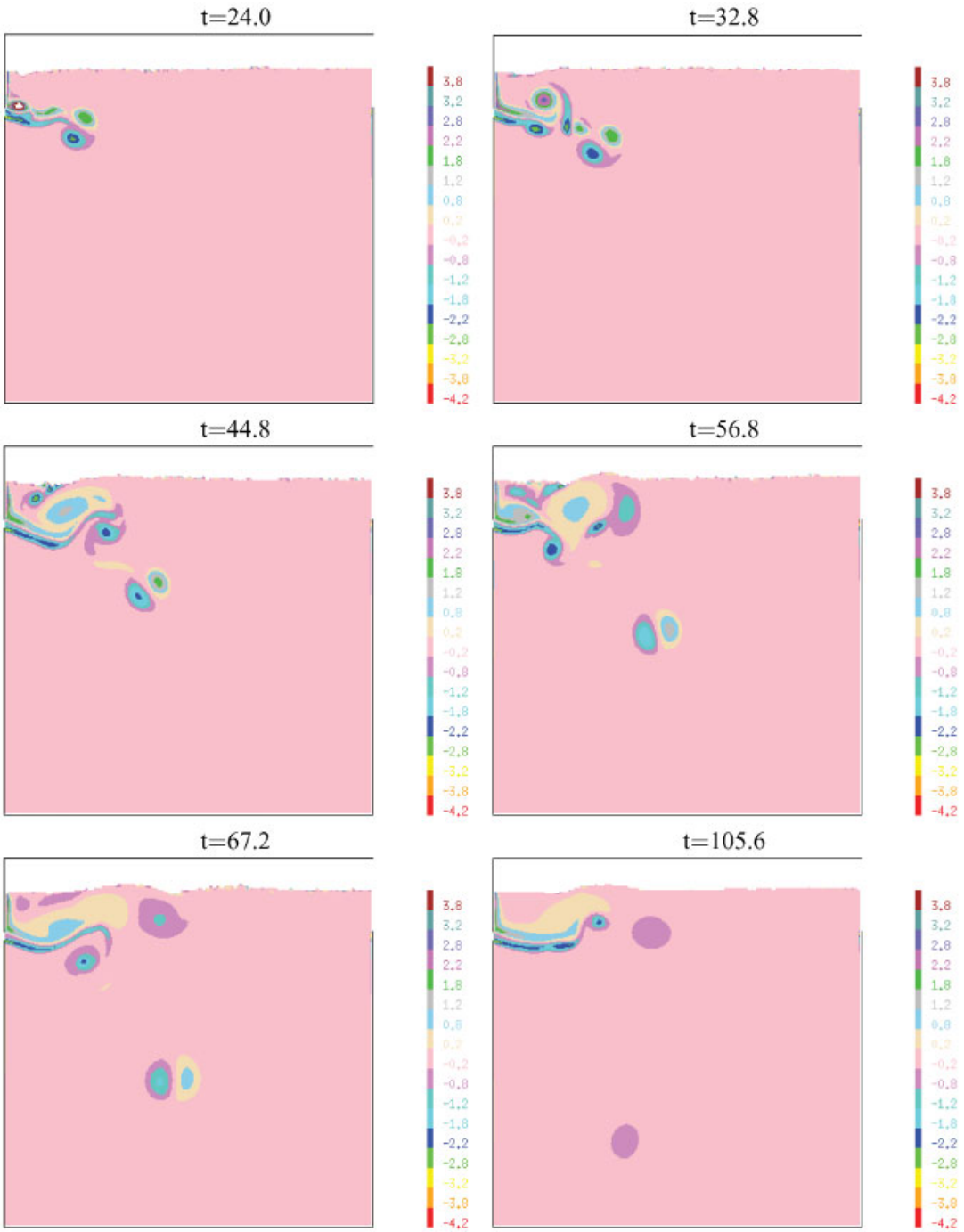

Plate 2. Non-dimensional time evolution of the non-dimensional vorticity contours of a two-dimensional numerical simulation, using the $H\,Re$ k–ε model. $H = 1.0$ m.

Copyright © 2004 John Wiley & Sons, Ltd.

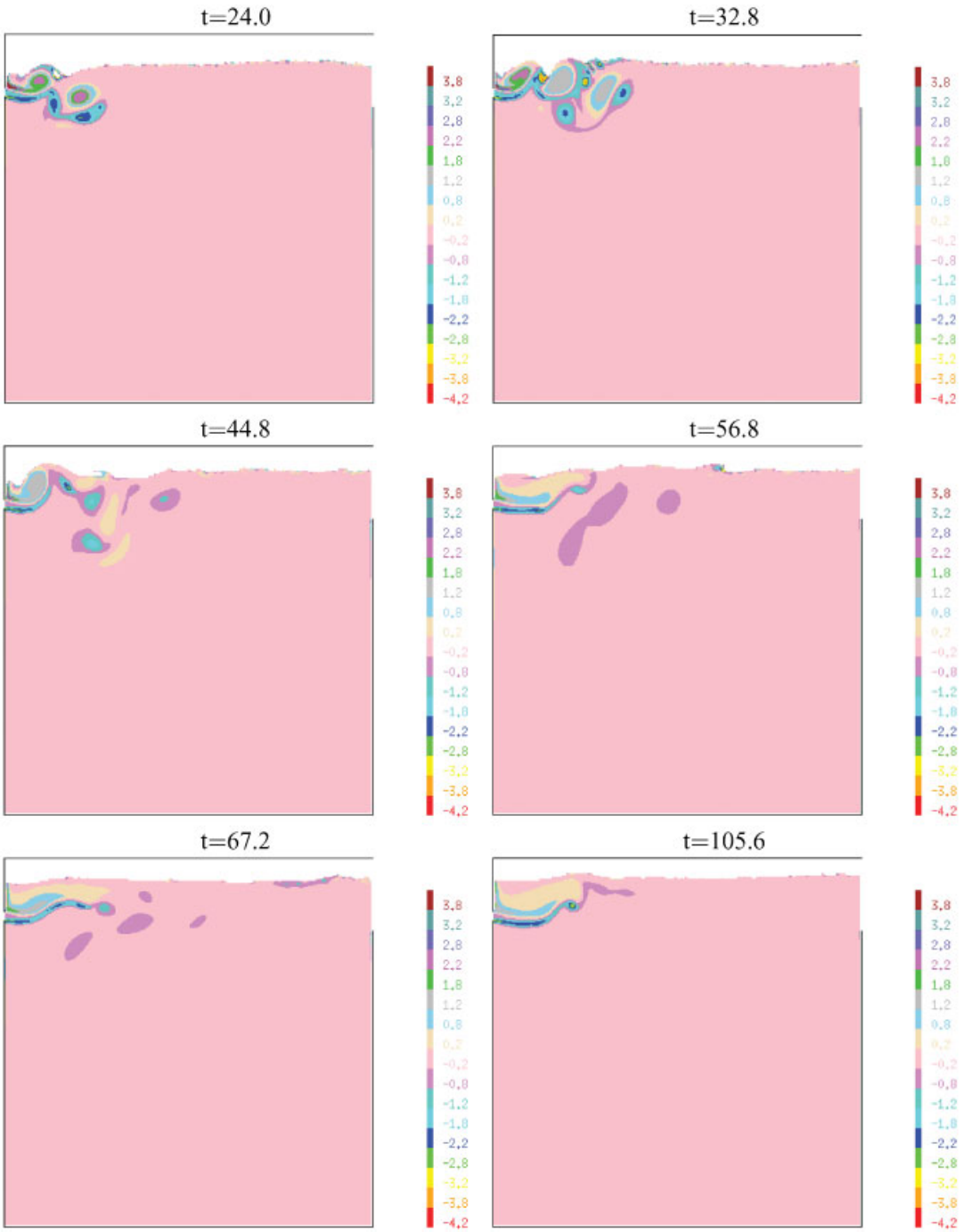

Plate 3. Non-dimensional time evolution of the non-dimensional vorticity contours of a two-dimensional numerical simulation, using the $H\,Re$ k–ε model. $H = 0.5$ m.

Copyright © 2004 John Wiley & Sons, Ltd.